AD_____

GRANT NUMBER DAMD17-94-J-4126

TITLE: Development of Efficient Dynamic Magnetic Resonance
Imaging Methods with Application to Breast Cancer Detection and
Diagnosis

PRINCIPAL INVESTIGATOR: Jill M. Hanson
                          Dr. Paul Lauterbur

CONTRACTING ORGANIZATION: University of Illinois
                           Urbana, Illinois 61801

REPORT DATE: August   1997

TYPE OF REPORT: Final

PREPARED FOR: Commander
                U.S. Army Medical Research and Materiel Command
                Fort Detrick, Frederick, Maryland 21702-5012

DISTRIBUTION STATEMENT: Approved for public release;
                         distribution unlimited

The views, opinions and/or findings contained in this report are
those of the author(s) and should not be construed as an official
Department of the Army position, policy or decision unless so
designated by other documentation.

19971230 047

1

REPORT DOCUMENTATION PAGE

Public reporting burden for this collection of information is estimated to average 1 hour per response, including the time for reviewing instructions, searching existing data sources, gathering and maintaining the data needed, and completing and reviewing the collection of information. Send comments regarding this burden estimate or any other aspect of this collection of information, including suggestions for reducing this burden, to Washington Headquarters Services, Directorate for Information Operations and Reports, 1215 Jefferson Davis Highway, Suite 1204, Arlington, VA 22202-4302, and to the Office of Management and Budget, Paperwork Reduction Project (0704-0188), Washington, DC 20503.

1. AGENCY USE ONLY *(Leave blank)*	2. REPORT DATE August 1997	3. REPORT TYPE AND DATES COVERED Final (1 Sep 94 - 31 Aug 97)

4. TITLE AND SUBTITLE Development of Efficient Dynamic Magnetic Resonance Imaging Methods with Application to Breast Cancer Detection and Diagnosis

5. FUNDING NUMBERS

DAMD17-94-J-4126

6. AUTHOR(S)

Jill M. Hanson

Dr. Paul Lauterbur

7. PERFORMING ORGANIZATION NAME(S) AND ADDRESS(ES)

University of Illinois
Urbana, Illinois 61801

8. PERFORMING ORGANIZATION REPORT NUMBER

9. SPONSORING/MONITORING AGENCY NAME(S) AND ADDRESS(ES)

Commander
U.S. Army Medical Research and Materiel Command
Fort Detrick, MD 21702-5012

10. SPONSORING/MONITORING AGENCY REPORT NUMBER

11. SUPPLEMENTARY NOTES

12a. DISTRIBUTION / AVAILABILITY STATEMENT

Approved for public release; distribution unlimited

12b. DISTRIBUTION CODE

13. ABSTRACT *(Maximum 200*

The goal of this predoctoral fellowship research project is to improve the temporal and spatial resolutions in dynamic contrast-enhanced magnetic resonance imaging of the breast. Specifically, we investigated the use of non-Fourier encoding for collecting the reduced encoding dynamic data sets. The conclusion from our study was that the current wavelet and SVD encoding methods do not achieve the desired goal of exploiting the desirable truncation properties of these basis functions and, at times, can introduce dangerous artifacts. For Fourier-encoded data, the Reduced-encoding Imaging by Generalized-series Reconstruction (RIGR) method was shown to be a better way to extrapolate the unmeasured dynamic data using *a priori* constraints than Fourier-keyhole. Next, we further optimized the basis functions of the generalized-series (GS) model used by the RIGR algorithm. The Two-reference RIGR (TRIGR) method resulted from suppressing background information in the GS basis functions, enabling them to better represent the regions of dynamic change. Explicit edge constraints derived from the reference image were then used with contrast information from the dynamic data to inject dynamic information into the GS basis functions. Finally, the problem of motion in dynamic imaging was addressed using a similarity norm to accurately detect the motion in spite of contrast changes and the low-resolution nature of the dynamic data.

14. SUBJECT TERMS Magnetic Resonance, Dynamic Imaging, Image Reconstruction, Constrained Image Reconstruction, Generalized Series, Inverse Problems, Breast Cancer

15. NUMBER OF PAGES
48

16. PRICE CODE

17. SECURITY CLASSIFICATION OF REPORT	18. SECURITY CLASSIFICATION OF THIS PAGE	19. SECURITY CLASSIFICATION OF ABSTRACT	20. LIMITATION OF ABSTRACT
Unclassified	Unclassified	Unclassified	Unlimited

NSN 7540-01-280-5500

Standard Form 298 (Rev. 2-89)
Prescribed by ANSI Std. Z39-18
298-102

FOREWORD

Opinions, interpretations, conclusions and recommendations are those of the author and are not necessarily endorsed by the U.S. Army.

____ Where copyrighted material is quoted, permission has been obtained to use such material.

____ Where material from documents designated for limited distribution is quoted, permission has been obtained to use the material.

____ Citations of commercial organizations and trade names in this report do not constitute an official Department of Army endorsement or approval of the products or services of these organizations.

____ In conducting research using animals, the investigator(s) adhered to the "Guide for the Care and Use of Laboratory Animals," prepared by the Committee on Care and Use of Laboratory Animals of the Institute of Laboratory Resources, National Research Council (NIH Publication No. 86-23, Revised 1985).

____ For the protection of human subjects, the investigator(s) adhered to policies of applicable Federal Law 45 CFR 46.

____ In conducting research utilizing recombinant DNA technology, the investigator(s) adhered to current guidelines promulgated by the National Institutes of Health.

____ In the conduct of research utilizing recombinant DNA, the investigator(s) adhered to the NIH Guidelines for Research Involving Recombinant DNA Molecules.

____ In the conduct of research involving hazardous organisms, the investigator(s) adhered to the CDC-NIH Guide for Biosafety in Microbiological and Biomedical Laboratories.

_____   8/12/97
PI - Signature   Date

3

Contents

4 Introduction

This predoctoral fellowship research project is concerned with the problem of dynamic magnetic resonance imaging (MRI). The potential application of dynamic MRI to breast cancer is to repeatedly image the breast following injection of a contrast agent. The interest in this lies in the possibility that breast tumors could be characterized noninvasively using both the temporal enhancement curve in the lesion as well as the spatial pattern of enhancement in the lesion [1–9]. This application would require high temporal resolution in the sequence of images, since the period of greatest differentiation between malignant and benign tumors is the first one or two minutes following injection of the contrast agent [10, 11]. In addition, high spatial resolution is imperative so that small tumors will not be missed. The ability to acquire rapid, high-quality images would also have application in monitoring the effects of treatment [12] and watching for recurrence [13].

However, with the conventional MRI technique, the requirements for obtaining high spatial and temporal resolutions are conflicting. For example, if the Fourier reconstruction method is used, the spatial resolution will be $1/(M\Delta k)$ where M is the number of encodings acquired and Δk is the step between data points in the spatial frequency space (commonly called k-space [14]). In this case, the temporal resolution will be limited to MT_R where T_R is the time to collect one encoding, which may not be sufficient if a large M is used to obtain high spatial resolution. Clearly, the temporal resolution can be improved by either reducing T_R or reducing M. The first strategy leads to fast-scan techniques, which try to acquire a full data set in a time that is short compared to the dynamic process. However, these techniques may require specialized hardware and have a reduced signal-to-noise (SNR) ratio. In addition, there may be power deposition problems in dynamic imaging due to the sequence of images that are acquired. The second strategy leads to reduced-scan techniques. The data acquisition strategy of many of these techniques is illustrated in Fig. 1. A high-resolution reference data set is acquired, usually with standard phase encoding, followed by a sequence of reduced dynamic data sets during the dynamic imaging period. To avoid the loss of spatial resolution that can occur with the reduced number of encodings, many of these techniques use *a priori* information in the data acquisition or image reconstruction steps. This research project

5

involves a systematic evaluation of the advantages and limitations of these reduced-scan methods, as well as the development of several techniques to improve the Reduced-encoding Imaging by Generalized-series Reconstruction (RIGR) method [15, 16].

5 Completed Research

5.1 Reduced-Encoding Data Acquisition

With the tremendous flexibility of MRI, it is natural to wonder if there is a better way to collect the information than by using the infinite complex exponential basis functions of the standard Fourier or phase encoding method. This is the motivation behind the wavelet [17–41] and singular value decomposition (SVD) [42–54] methods, which use a wavelet decomposition or the SVD of a reference image to determine the reduced encoding vector set. The former method is of interest due to the localized nature of wavelet basis functions, and the latter is of interest due to the fact that the truncated SVD is the optimal truncated representation of a matrix (in the least squares error sense) [55]. The hope is that, by using these basis sets, the image can be well-represented with fewer encoding vectors than is possible with Fourier encoding. For this reason, the wavelet and SVD encoding methods were investigated in comparison to phase encoding for dynamic imaging applications.

The wavelet and SVD encoding methods use the following steps to try to exploit the desirable truncation properties of the encoding vector sets:

1. Acquire a high-resolution reference data set using phase encoding and reconstruct using the Fourier reconstruction method.

2. Decompose the reference image using the appropriate basis set (either the chosen wavelet basis set or the SVD).

3. Select the "most significant" encoding vectors from the decomposition of step 2. For the wavelet encoding method, the truncated set is chosen based on the largest reference wavelet coefficients. For the SVD encoding method, the truncated set is chosen based on the largest reference singular values.

4. Use the selected set of encoding vectors from step 3 to acquire the reduced-encoding dynamic data set using spatially selective RF excitation pulses.

5. Reconstruct the dynamic image using the appropriate synthesis procedure (the inverse wavelet transform or SVD synthesis).

Note that with the wavelet encoding method, the choice of wavelet basis set will affect the results due to implementation issues, as well as the ability to represent the dynamic image with a truncated basis set. In selecting a particular wavelet basis set for experimental MR encoding, a smoother wavelet is preferred, because it requires a shorter RF pulse [24] and reduces the bandwidth requirement of the RF pulse [36]. In addition, a more accurate wavelet-shaped profile can be excited, which will result in better images [24]. However, there is a trade-off between the length of the required RF pulse and the spatial support of the wavelet. This research utilized the orthogonal[1] Daubechies D18 wavelet basis set [56] and the biorthogonal Cohen 7/9 wavelet basis set [57], which are considered by many to be among the best for image compression [58]. This research focused on the theoretical power of the basis set for encoding dynamic images and chose to ignore the long RF pulse that would be required to excite the profiles associated with these wavelets.

It is important to note that the simulations in this study did not take into account several factors that would degrade the performance of the non-Fourier encoding methods. First, it was assumed that the spatially selective RF encodings could be exactly excited. This is difficult in practice, and imperfect excitation will degrade the resulting image [24, 51]. In addition, T_1 variations across the image will further distort the encoded profile when a short T_R is used, which is especially a problem when a T_1 contrast agent is injected. The use of RF encoding with the non-Fourier methods also limits the application to single slice or 3D spin echo imaging, and it is not easy to implement 2D or thin slab 3D gradient echo sequences [45]. Another point is the signal-to-noise ratio (SNR) loss due to the use of spatially selective excitation for the non-Fourier encoding methods [24, 31]. These problems do not arise with Fourier encoding, which uses linear gradients to encode the image information rather than spatially selective excitation.

In addition, the non-Fourier encoding methods described here use the reference data

---

[1]Orthogonal and biorthogonal wavelets are the two main classes of traditional wavelets.

set to choose the encoding vectors for the entire dynamic imaging period. A modification of this technique is to use a reconstructed dynamic image to select the encodings for the subsequent dynamic image. Although this should help to increase the similarity between the image used to truncate the encoding vector set and the image acquired with the selected dynamic encodings, it would reduce the achievable temporal resolution due to the computation and magnet setup required between successive dynamic data sets.

As discussed earlier, the truncated wavelet and SVD representations have the desirable property of representing an image well with fewer encodings than are necessary with the Fourier representation. To exploit these desirable properties for reduced-encoding dynamic imaging, the current methods use a reference image to guide the truncation of the set of encoding vectors. The danger in doing that is that the selected encodings may not be optimal for the representation of the dynamic image and, at times, the reference-based truncation can introduce dangerous artifacts. To illustrate this, simulations of two important dynamic breast imaging applications, a contrast-enhanced dynamic study and an interventional MRI needle biopsy procedure, are shown below.

Figure 2 shows the different reduced-encoding methods applied to the breast simulation developed for this project. The dynamic changes between the reference and dynamic images include a variable rate of enhancement in each of the "lesions" as well as a slow overall increase in the background "tissue". Figures 2(a)-(b) are the reference and dynamic images, respectively, reconstructed using 128 phase encodings. Figure 2(c) shows the dynamic image reconstructed using the 16 phase encodings from the center of k-space. Figures 2(d)-(e) show the dynamic image reconstructed using 16 orthogonal and biorthogonal, respectively, wavelet encoding vectors. Figure 2(f) shows the dynamic image reconstructed using 16 SVD encoding vectors. The average signal magnitude in the four lesions for each of the methods is quantified in Fig. 3. Note that the SVD method assigns nearly the same signal magnitude to all four lesions in the dynamic image, as is the case in the reference image. This is obviously undesirable for this application since the goal is to accurately track the spatial and temporal variation of the signal magnitude in the lesions.

An interventional MRI needle biopsy procedure is illustrated in Fig. 4. Figures 4(a)-(b) are the reference and dynamic images, respectively, reconstructed using 256 phase

encodings. Note the additional dark line feature in the dynamic image, supposedly created by the insertion of a biopsy needle. The arrow indicates the center of the needle track. Figures 4(c)-(f) were reconstructed using 32 encodings with phase encoding, orthogonal wavelet encoding, biorthogonal wavelet encoding, and SVD encoding, respectively. In the phase encoded image, Gibbs ringing results from the sharp needle feature as would be predicted by Fourier theory. The wavelet encoding method results in a blurred needle reconstruction. In the SVD image, note the apparent displacement of the reconstructed needle from the proper position. This is a dangerous artifact since, for this application, the purpose of MRI is to ensure that the lesion is biopsied, as opposed to the surrounding normal breast tissue.

The artifacts seen with the wavelet and SVD encoding methods are not due to the truncation of the basis sets, but are due to the particular encoding vectors that are selected based on the reference image. This is illustrated in Figs. 5(a)-(c) which show the dynamic image reconstructed using the optimal orthogonal wavelet, biorthogonal wavelet and SVD encoding vectors, i.e., the encoding vectors selected based on the dynamic image itself, as opposed to the reference image. The greatly improved reconstruction of the needle over that seen in Figs. 4(d)-(f), respectively, attests the non-optimality of the reference-based truncation.

Based on this work, we have shown that, if the *a priori* information that is available is a reference image, the current wavelet and SVD encoding methods do not achieve the desired result of exploiting the desirable truncation properties of these basis sets, and, at times, can result in undesirable artifacts. For this reason, we continue to use phase encoding to collect the reduced encoding dynamic data sets.

5.2 Reduced-Encoding Image Reconstruction

Given that the available reduced encoding dynamic data sets are Fourier encoded data, several available image reconstruction techniques were investigated, including zero-padded Fourier series, the Fourier-keyhole method[2] [59,60], and the Reduced-encoding Imaging by Generalized-Series Reconstruction (RIGR) method [15,16].

---

[2]The keyhole method can also be used with the wavelet and SVD [51] encoding methods, although that will not be discussed here since we are only considering phase encoding at this point.

The zero-padded Fourier series simply replaces the unmeasured dynamic data with zeros, whereas the Fourier-keyhole method directly replaces the unmeasured dynamic data with the corresponding reference data. The data sets thus created are input to the inverse Fourier transform for reconstruction. Note that, although the resulting images may look quite different, the zero-padded Fourier series and Fourier-keyhole methods follow the dynamic changes at the same low resolution. On the other hand, the RIGR method uses a generalized-series (GS) model to reconstruct the dynamic changes at a higher resolution than is possible with the zero-padded Fourier series or Fourier-keyhole techniques. The generalized-series model can be expressed as [15]

$$I_{\text{dyn}}(x) = I_{\text{ref}}(x) \sum_{n=-N/2}^{N/2-1} c_n e^{i2\pi n \Delta k x} \tag{1}$$

where $I_{\text{ref}}(x)$ is the reference image and N is the number of dynamic encodings. The coefficients c_n are obtained by fitting the dynamic data to the following equation to maintain data consistency [15]

$$d_{\text{dyn}}(m) = \sum_{n=-N/2}^{N/2-1} c_n d_{\text{ref}}(m - n) \tag{2}$$

where $d_{\text{ref}}(m-n)$ is the reference data. Plugging these coefficients into Eq. (1) will yield the desired dynamic image.

Typically, imaging methods are compared using a point spread function (PSF) analysis, which gives a measure of the attainable spatial resolution of a method. However, with constrained reconstruction methods such as RIGR, the PSF will depend not only on the number of dynamic encodings available, but also on the reference image that is used. Therefore, the methods were compared using a generalized point spread function analysis which investigated the reconstruction of a point change using a boxcar reference image. The width of the boxcar, the location of the point change and the number of dynamic encodings were varied to determine the affect of these factors on the generalized PSF width. An example of the results are shown in Fig. 6 rows 1-3 for a centered point change, a point change shifted one-fourth the width of the boxcar from the center, and a point change shifted just under one-half (0.49) the width of the reference boxcar from the center, respectively. In the case shown, the width of the reference boxcar was

0.03125 (FOV=1), but only the center fourth of the plot is shown for better visualization. Also note that (a)-(c) are on a different scale than (d)-(e). In all rows, (a)-(c) are the reference function, the dynamic image, and the point change, respectively, reconstructed using 512 phase encodings. Plots (d)-(e) show the point change reconstructed using Fourier-keyhole (or, equivalently, zero-padded Fourier series) and RIGR, respectively, using eight dynamic encodings. Although the reference boxcar contains no edge information about the point change, nearby edges help constrain the reconstruction of the point change in the RIGR technique.

The relationship between the number of dynamic encodings and the width of the generalized PSF for the centered point change case is shown in Fig. 7 for Fourier-keyhole and for RIGR with a reference boxcar of various widths. The GS approach used in RIGR results in a narrower generalized PSF for all reference boxcar widths and for all numbers of dynamic encodings. As the width of the reference boxcar approaches the FOV, the generalized PSF width of the RIGR method approaches that of the zero-padded Fourier series reconstruction. This is expected since, in this case of no effective *a priori* information, the GS reduces to the Fourier series.

Figure 8 shows the relationship between the width of the generalized PSF and the width of the reference boxcar for Fourier-keyhole (or zero-padded Fourier series) and for the RIGR method with various locations of the point change. Note that the width of the generalized PSF decreases with the width of the reference boxcar and also with greater proximity of the point change to a boxcar edge regardless of the width of the reference boxcar for the RIGR method. This is another illustration of how nearby edges in the reference image help constrain the reconstruction of the point change with the RIGR method.

If the reference boxcar does contain edge information for the point change, the generalized PSF obtained with RIGR can be further improved. This is illustrated in Fig. 9 in which rows 1-3 show the case of a point change that is centered, shifted by one-fourth the reference boxcar width from the center, or shifted by just under one-half (0.49) the reference boxcar width from the center, respectively. Plots (a)-(d) show the baseline reference, active reference, dynamic image, and point change (the change between the baseline reference and the dynamic image), respectively, reconstructed with 512 phase

11

encodings. Plot (e) shows the point change reconstructed using RIGR with the active reference image and eight dynamic encodings. The edge information for the point change in the active reference image helps to further reduce the width of the generalized PSF.

The effects of the narrower PSF obtained with the RIGR method can be seen in the reconstruction of dynamic changes in MRI images. This is illustrated in Fig. 10 in which (a)-(c) are the reference image, the dynamic image, and the difference between the two images, respectively, reconstructed using 256 phase encodings. Figure 10(d)-(e) show the difference image reconstructed using Fourier-keyhole (or the zero-padded Fourier series) and RIGR, respectively, using 32 dynamic encodings. Note the improved reconstruction of the dynamic changes with RIGR.

In addition, image artifacts can arise from the use of Fourier-keyhole due to inconsistency between the reference and dynamic data sets. With RIGR, the GS model guarantees a $(N-1)^{th}$ order continuity between the measured and extrapolated data if N dynamic encodings are used [16]. On the other hand, with Fourier-keyhole in which the reference data is simply pasted onto the dynamic data, there is no guarantee of data consistency. This is especially a problem in contrast-enhanced dynamic imaging in which the contrast agent can cause an overall background signal increase as well as localized increases in the tumor regions. The nature of the artifacts will depend on whether the reference image is more or less enhanced than the dynamic image. The latter case is shown in Fig. 11 in which (a)-(b) are the reference and dynamic images, respectively, reconstructed using 256 phase encodings. Figures 11(c)-(d) show the dynamic image reconstructed using 16 dynamic encodings using Fourier-keyhole and RIGR, respectively. Note the edge-type artifacts in the Fourier-keyhole image which are not visible in the RIGR image.

This work has shown that, for image reconstruction with Fourier encoding, the RIGR method is the best way to extrapolate the unmeasured data using the *a priori* constraints due to the higher resolution tracking of the dynamic changes and the reduced data inconsistency artifacts. The remainder of the project focused on further improvements to the RIGR technique.

5.3 Two Reference RIGR (TRIGR)

The two reference RIGR (TRIGR) method was developed as an offshoot from the original research proposal. The TRIGR method results in improved dynamic images over the original RIGR method due to suppression of the background information through the use of a second high-resolution reference image. As a result, the GS basis functions need only represent the areas of change and not the static parts of the image. Consequently, the method directly reconstructs an image of the dynamic changes. If the dynamic image itself is desired, it can simply be obtained by adding the dynamic change image to the baseline reference image.

Specifically, the data acquisition procedure for the TRIGR method involves the following steps which are illustrated pictorially in Fig. 12:

1. Acquire a high-resolution baseline reference data set in which the number of encodings is determined by the desired spatial resolution.

2. Acquire a sequence of low-resolution dynamic data sets in which the number of encodings is chosen with respect to the desired temporal resolution.

3. Acquire a high-resolution active reference data set.

Note that the active reference data set need not be acquired at the end of the dynamic imaging period, but can be obtained at any appropriate point in the experimental procedure. For some applications, it may be desirable to acquire reference data sets at various points during the experimental protocol, and then use the appropriate two reference data sets to reconstruct a given dynamic image. This is especially attractive since the reconstructed dynamic image improves as the active reference image becomes more similar to the dynamic image.

Reconstruction of the dynamic images is accomplished using the generalized series model with a reference image in which the background has been suppressed. Specifically, the reconstruction steps are:

1. Construct the difference reference image by subtracting the full baseline and active reference data sets and reconstructing using the traditional Fourier method.

2. Create the dynamic difference data by subtracting from the dynamic data the corresponding encodings of the baseline reference image, namely

$$d_{\text{diff}}(x) = d_{\text{dyn}}(k) - \hat{d}_{\text{baseline}}(k) \tag{3}$$

where $d_{\text{dyn}}(k)$ is the dynamic data and $\hat{d}_{\text{baseline}}(k)$ represents the corresponding baseline reference encodings.

3. The GS model then becomes

$$I_{\text{diff}}(x) = I_{\text{ref}}(x) \sum_{n=-N/2}^{N/2-1} c_n e^{i2\pi n \Delta k x} \tag{4}$$

where $I_{\text{ref}}(x)$ is the difference reference image of step 1 and N is the number of dynamic encodings. The coefficients c_n are obtained by fitting the difference data of Eq. (3) to the following equation to maintain data consistency

$$d_{\text{diff}}(m) = \sum_{n=-N/2}^{N/2-1} c_n d_{\text{ref}}(m - n) \tag{5}$$

where $d_{\text{ref}}(m - n)$ is the difference data created by subtracting the baseline and active reference data sets. Plugging these coefficients into Eq. (4) will yield the reconstructed dynamic difference image.

4. If the dynamic image itself is desired, it can be generated by adding the complex dynamic difference image of step 3 to the baseline reference image, i.e.,

$$I_{\text{dyn}}(x) = I_{\text{baseline}}(x) \quad + \quad I_{\text{diff}}(x) \tag{6}$$

where $I_{\text{baseline}}(x)$ is reconstructed using the standard Fourier technique with the full set of baseline reference encodings.

The effect of the background suppression provided by the TRIGR method can be seen in the generalized PSF. Figures 13(a)-(c) are the baseline reference, active reference and dynamic images, respectively, reconstructed using 512 phase encodings. Figures 13(d)-(e) show the ideal point change reconstructed with 512 phase encodings and the point change reconstructed using TRIGR with 8 dynamic encodings, respectively. The improvement due to the background suppression can be seen by comparing Fig. 13(e) to

14

Fig. 9(e). Although the reference image in the TRIGR technique contains no additional information about the point change than the active reference image used with the RIGR method in Fig. 9, the background suppression improves the reconstructed generalized PSF.

Of course, this is the ideal case of complete background suppression. As the background information is less effectively suppressed, the improvement obtained through using TRIGR will not be as great. This is illustrated in Figs. 14 and 15 which show cases of complete and incomplete background suppression, respectively, in the breast simulation developed for this project. In both figures, (a)-(c) are the precontrast reference, postcontrast reference and dynamic images, respectively, reconstructed using 128 phase encodings. Images (d)-(e) are the dynamic image reconstructed using the original RIGR method with the precontrast and postcontrast reference images, respectively, and 16 dynamic encodings. Image (f) is the dynamic image reconstructed using the TRIGR method with 16 dynamic encodings. As can be seen through comparison of Figs. 14(d)-(f) and Figs. 15(d)-(f), the improvement obtained through the use of the TRIGR method is greater as the background information is more completely suppressed.

The effect of this improved PSF can be seen in dynamic MR images. Figure 16 shows images obtained from a dynamic contrast-enhanced data set of a rat with a large breast tumor (data provided by Dr. Erik Wiener of Dr. Paul Lauterbur's group). A spin echo sequence (TR300/TE20) was used to collect a high-resolution baseline reference data set. The contrast agent was then injected and a sequence of dynamic data sets was collected as the contrast agent washed into the tumor. A second reference data set was then collected while the contrast agent was still strongly visible in the slice. Figures 16(a)-(b) show the baseline and active reference images, respectively, and (c) shows the difference between the dynamic image (not shown) and the baseline reference image. These three images were reconstructed using 256 phase encodings. Figures 16(d)-(f) show the difference image reconstructed with 8 dynamic encodings using Fourier-keyhole, the original RIGR method, and the TRIGR method, respectively. In the TRIGR image, note the improved delineation of the internal details of the tumor, such as those indicated by the arrows. In this case, the temporal resolution could be improved 32-fold (256/8) while maintaining high quality in the dynamic image through the use of the TRIGR method.

5.4 RIGR/TRIGR with Explicit Edge Constraints

Since the GS model has a limited number of terms (see Eq. 1), the dynamic change that is "registered" on the reference image may not be high-resolution. Therefore, in order to improve the reconstruction of the dynamic image, it is desirable to inject dynamic information into the GS basis functions, as opposed to deriving them solely from the reference information. If the contrast behavior of the reference image is the same as that of the dynamic image, it is useful to use this information in the GS basis functions. On the other hand, if the contrast behaviors are different, it would be better to use only the edge information from the reference image and to derive the contrast information from the dynamic data. In order to do this, two steps are required: the determination of the boundary locations and the incorporation of this information into the GS basis functions.

To determine the location of the edges, it is desirable to use a multiscale approach since the edges in an MRI image are expected to occur at different scales. Two available methods of doing that are wavelet edge detection [61–63] and the multiresolution edge detection approach [64, 65]. The concepts of scale in the two methods are slightly different. In the wavelet edge detection methods, the idea of scale relates to the size of the edge itself, whereas in the multiresolution approach, scale relates to both physical proximity and greyscale "closeness". Another difference is that the multiresolution approach does not involve an *a priori* model of the edge, which is beneficial since the shape of the edges in MR images are not known *a priori*. For this application, the multiresolution approach was selected because it resulted in more continuous edges and detected edges which were missed by the wavelet edge detection approach.

Various methods were investigated for incorporating the edge information from the reference image and the contrast information from the dynamic data into the GS basis functions. These included fitting various basis function sets to the regions defined by the edges, including the Haar and Daubechies D20 wavelets and the localized polynomial approximation (LPA) [66]. The results of these fitting steps were used either as the new reference image or used to scale the reference image. However, even the most promising of these techniques, the LPA approach, resulted in a smoothing effect, because the number of regions had to be limited to obtain reliable fitting with the small amount of dynamic data available.

16

To alleviate this problem, the proposed method calculates the average signal difference in each region detected in the reference image using the dynamic data and the corresponding encodings of the reference data. Therefore, since no fitting step is required, all of the regions can be used which reduces the blurring effect. In addition, since the method is used to calculate the difference image as opposed to directly calculating the new reference image, the effect of edges that are missed or slightly off will be reduced.

Specifically, the steps for applying this method during the reconstruction of the dynamic image are:

1. Reconstruct the high-resolution reference image and extract the regions using the multiresolution edge detection approach.

2. Reconstruct a zero-padded difference image from the low-resolution dynamic data and the corresponding encodings of the reference data using the Fourier reconstruction technique.

3. Impose the region structure from step 1 on the image of step 2 to determine the average signal magnitude difference in each of the regions.

4. The new reference image is then created as, for a baseline reference image,

$$\hat{I}_{\text{ref}} = I_{\text{ref}} + I_{\text{diff,ave}} e^{i \angle I_{\text{diff}}} \tag{7}$$

or, for an active reference image,

$$\hat{I}_{\text{ref}} = I_{\text{ref}} - I_{\text{diff,ave}} e^{i \angle I_{\text{diff}}} \tag{8}$$

where $I_{\text{diff,ave}}$ is the result of step 3 and $\angle I_{\text{diff}}$ is the phase of the zero-padded difference image of step 2.

The method can easily be incorporated into the TRIGR method by modifying the post-contrast reference image as described above.

The effects of applying this method to the contrast-enhanced dynamic imaging experiment conducted by Dr. Erik Wiener is shown in Fig. 17. Figures 17(a)-(b) are the

17

precontrast reference and dynamic images, respectively, reconstructed with 256 phase encodings. Figures 17(c)-(d) show the dynamic image reconstructed using eight dynamic encodings with the original RIGR method and the RIGR method with explicit edge information, respectively. Image (d) has a more accurate reproduction of the contrast behavior in the dynamic image than (c). However, some blurring can still be seen due to edges that are not detected in the precontrast reference image. This suggests that a postcontrast reference image should be used for the edge extraction step when possible because it may contain additional edges introduced by the dynamic changes. This is illustrated in Fig. 18 in which (a)-(b) are the postcontrast reference and dynamic images, respectively, reconstructed using 256 phase encodings. Figures 18(c)-(d) show the dynamic image reconstructed using the original RIGR method and the RIGR method with explicit edge information, respectively, with eight dynamic encodings. As expected, the postcontrast reference provides additional edges which reduces the blurring, as can be seen by comparing Fig. 17(d) and Fig. 18(d). However, in this case, the improvement in using explicit edge information is not as great as in the precontrast reference case, since the contrast behavior in the dynamic image is closer to that of the postcontrast reference image than that of the precontrast reference image. In any case, these examples illustrate that the use of this technique can improve the dynamic image quality while maintaining the improved temporal resolution available from the RIGR or TRIGR methods.

5.5 Motion Compensated Dynamic Imaging

Motion has long been a problem for MRI, because it destroys the encoding relationship between the signal and the location of the spins. With constrained reconstruction methods such as RIGR, additional artifacts can be created by motion which occurs between the acquisition of the reference and dynamic data sets, because the reference image may no longer be a valid constraint for the image reconstruction step. An approach to overcome this problem is to detect and correct the object motion before the constrained reconstruction step is performed. However, detection of object motion in reduced-encoding dynamic imaging is nontrivial due to several factors. First, dynamic image contrast changes and object motion are mixed together. This is especially a problem in contrast-enhanced dynamic imaging of the breast due to the large, rapid

contrast changes that can occur in the tumor regions. Second, the dynamic data sets are low-resolution, and it is usually necessary to detect motion to a higher accuracy than that dictated by the low-resolution Fourier pixel size. To overcome these problems, we propose to use a similarity norm which can accurately detect the motion in spite of the contrast changes and the low-resolution nature of the dynamic data. The similarity norm tries to remove the effects of the contrast change by using only the edges from the high-resolution reference image for the motion estimation.

The approach we propose assumes relative rigid-body motion which occurs between the acquisition of the reference and dynamic data sets. Possible methods of addressing the problem if these assumptions do not hold will be discussed at the end of this section. The proposed method is applied to a sequence of dynamic images in turn, so that the dynamic data set is compared to a high-resolution image that should have a more similar edge structure than the original reference image. First, the motion between the high-resolution reference image and the first dynamic data set is measured. These measurements are used to correct and reconstruct the first GS dynamic image. This high-resolution GS image is then used with the second dynamic data set to determine the motion that occurred between these two acquisition times. The cumulative motion measurements are used with the reference image to reconstruct the second GS dynamic image. This procedure is repeated for the entire image sequence. Note that the dynamic image is reconstructed using the original high-resolution reference image to reduce errors that could arise due to the accumulated motion correction.

As mentioned before, we assume that there is relative rigid-body motion between the low-resolution image I_2 and the high-resolution image I_1. In other words, the relationship between the images can be written as

$$I_2(x, y) \sim I_1(x \cos \theta_0 - y \sin \theta_0 + x_0, x \sin \theta_0 + y \cos \theta_0 + y_0) \qquad (9)$$

where the relative rigid-body rotation and translation are specified by x_0, y_0, and θ_0 and the tilde signifies that I_1 and I_2 can have different contrast behavior. Therefore, the goal of the motion-estimation step is to find x_0, y_0, and θ_0. Specifically, the following steps are used:

1. Reconstruct the high-resolution image I_1 using the Fourier reconstruction technique and segment it into a number of "homogeneous" regions. The strategy here is to use these region boundaries as landmark features.

2. Reconstruct the low-resolution image I_2 using the zero-padded Fourier reconstruction method.

3. Superimpose the region structure of step 1 onto the image of step 2 and calculate the regional intensity inhomogeneity σ_l^2, which is used as an indicator of the misalignment between the two images.

4. The misalignment error E_a is calculated as

$$E_a = \sqrt{\sum_{l=1}^{N_{\text{reg}}} \frac{m_l}{N} \sigma_l^2}, \tag{10}$$

where N_{reg} is the number of regions, m_l is the number of pixels in each region and N is the total number of pixels. Clearly, the value of E_a is a function of the motion parameters. E_a is minimized to find the values of x_0, y_0, and θ_0.

5. The estimated-motion parameters from step 4 are then used in the GS model as

$$\hat{I}_{\text{dyn}}(r) = T_{est} I_{\text{ref}}(r) \sum_{n \in \mathcal{N}_{\text{dyn}}} c_n e^{-i2\pi n \Delta k r}, \tag{11}$$

where T_{est} is the transformation that corresponds to the estimated-motion parameters.

The results of applying the proposed method to the contrast-enhanced dynamic study of a rat with breast cancer are shown in Fig. 19 in which (a) is the reference image that was reconstructed using 256 phase encodings. Images (b)-(d) were reconstructed using RIGR with 32 dynamic encodings. In image (b), there was no motion between the reference and dynamic data sets, and therefore, it represents the ideal RIGR reconstruction. The remaining images represent a case in which the position of the object during the dynamic data acquisition has changed from the reference position by a rotation of 3 degrees and shifts of 5 and -3 pixels in the phase encoding and frequency encoding directions, respectively. Figures 19(c)-(d) were reconstructed with no motion correction and with the proposed method, respectively. Note the reduced motion artifacts in the corrected image (d).

If it cannot be assumed that no appreciable motion occurs during the collection of a particular reduced-encoding dynamic data set, other methods will have to be employed to measure this intraset motion. One possible way to do that is by using navigator techniques [67] that acquire a "navigator echo" during each view in addition to the image information. Each navigator echo is then compared to an initial reference navigator echo using correlation [67] or a least squares technique [68–70] to determine the motion along the navigator direction. Additional navigator echoes can be used to measure motion in the other directions, or orbital navigator echoes [69] can be used to simultaneously measure the two directions of translation and rotation in a plane. Although the navigator techniques are being used in many applications, the methods cannot be directly applied to dynamic imaging, because the basic assumption of the navigator echo method will be violated; namely, that all of the changes in the navigator data are due to motion of the object. This causes a problem in contrast-enhanced dynamic imaging of the breast, as well as other dynamic imaging applications, in which the navigator data from each view can look very different even without motion, leading to incorrect motion estimates.

We considered trying to get around this by comparing a navigator to the immediately preceeding navigator to determine the motion parameters, as opposed to an initial reference navigator. However, although this should reduce the effect of the dynamic changes on the navigator data, the incremental motion may be too small to be detected with this method. Then, because the motion at a point in time would be the accumulation of the measured incremental motions up to that time, the error in the motion estimate may become quite large.

Perhaps a better way to use the navigator method with dynamic imaging applications is to design the pulse sequence such that the navigator signal is not sensitive to the contrast changes. For example, consider a contrast-enhanced dynamic study using a T_2 contrast agent. The T_2 contrast agent modifies the appearance of the tissues which take it up by changing the T_2 relaxation constant. Therefore, the image data should be sensitive to the change in T_2, but the effect of T_2 on the navigator data should be minimal. A possible way to accomplish this is to acquire the FID signal following the RF excitation pulse as the navigator data and use the echo signal as the image data. In this way, the image can be T_2 weighted, but the navigator signal will be proton density weighted. This method would require careful design of the pulse sequence with

the given application in mind. The optimal solution for dynamic imaging may be a combination that utilizes the strengths of both the navigator method and the similarity norm technique.

In many cases, the motion may occur in three dimensions, as opposed to the planar motion discussed here. In this case, the solution will depend upon whether the imaging sequence is acquiring 2D slices or a 3D volume. In the case of 2D slices, the excitation and signal reception locations will need to be dynamically adapted based on the detected motion perpendicular to the imaging plane [71]. The in-plane motion can then be addressed, as discussed previously. For 3D imaging, the motion detection scheme would have to be expanded to detect all six degrees of motion (three translations and three rotations).

6   Conclusions

The goal of this predoctoral fellowship research project is to obtain simultaneously high temporal and spatial resolutions in reduced-encoding contrast-enhanced dynamic imaging of the breast. As can be noted, the project expanded from the original proposal as I progressed through my graduate studies. The contributions of this work include:

1. The issues involved in reduced-encoding data acquisition were analyzed with the conclusion that the use of a reference image as the *a priori* information to guide the reduced-encoding data acquisition process does not achieve the goal of exploiting the desirable truncation properties of the non-Fourier basis sets and, at times, can create dangerous artifacts.

2. The RIGR method was shown to result in higher resolution tracking of the dynamic changes and reduced data inconsistency artifacts when compared to the zero-padded Fourier series or Fourier-keyhole methods.

3. The TRIGR method was developed which uses the additional information available from a second high-resolution reference image to suppress the background information in the GS basis functions, resulting in improved dynamic images with minimal increase in imaging time. Dr. Noam Alperin and Dr. Michelle Vaughan at the

University of Illinois at Chicago have begun an investigation into the application of the TRIGR technique to human contrast-enhanced dynamic breast imaging, in collaboration with Dr. Paul Lauterbur's group at the University of Illinois at Urbana-Champaign. However, as of the date of this report, no data involving contrast-enhanced dynamic imaging of human breast cancer was yet available for my use.

4. A technique was developed to inject dynamic information into the GS basis functions, as opposed to deriving them solely from the reference image, through the use of explicit edge information. The method can help improve the reproduction of the contrast behavior in the dynamic images.

5. A method was proposed for accurately detecting the motion between the reference and dynamic data sets in spite of the contrast changes and the low-resolution nature of the dynamic data.

And last, but not least, I successfully completed the requirements for my Ph.D. in electrical engineering while working on this predoctoral fellowship research project. I am very grateful for the opportunity that was afforded me by the Army Breast Cancer Research Program. The financial support, as well as the opportunity to work on such an exciting project these last three years, are deeply appreciated.

Reference data
M encodings

Dynamic data
N encodings
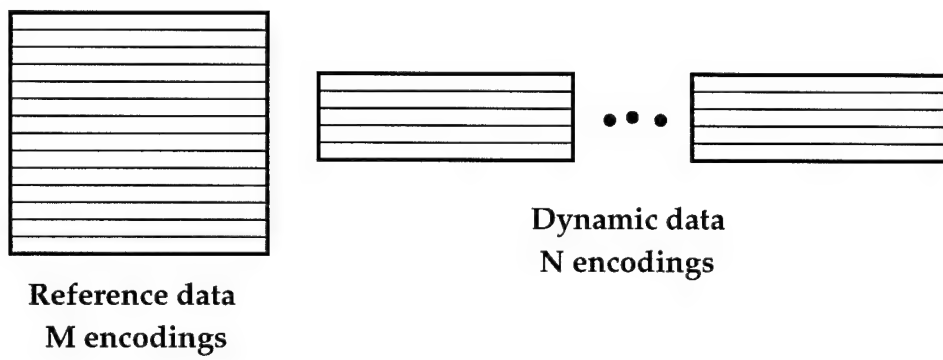
Figure 1: Data Acquisition Strategy for Reduced-encoding Techniques
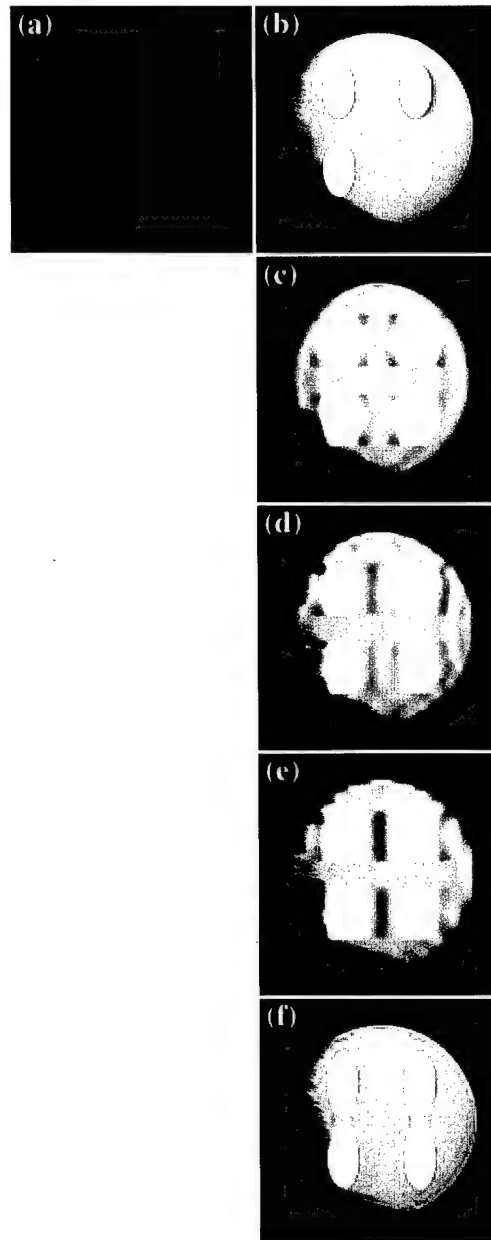
Figure 2: Non-Fourier Encoding Applied to Contrast-Enhanced Imaging: (a)-(b) The reference and dynamic images, respectively, reconstructed using 128 phase encodings. The remaining images were reconstructed with 16 dynamic encodings using different encoding methods: (c) phase (Fourier), (d) orthogonal wavelet, (e) biorthogonal wavelet and (f) SVD. The phase, wavelet and SVD encoding directions are vertical. Note that the SVD method assigns nearly the same signal magnitude to all four lesions.
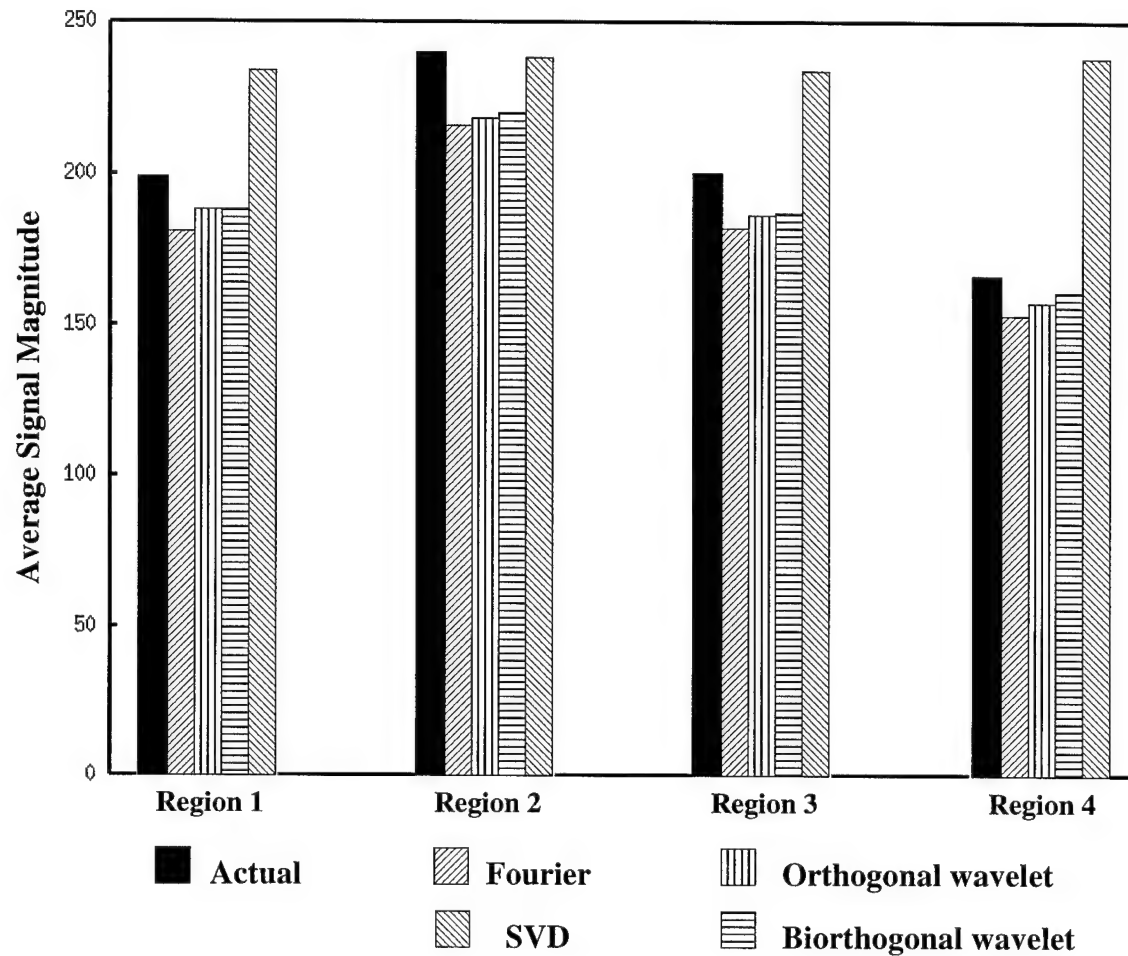
Figure 3: Average Signal Magnitude of the Lesions of Fig. 2(b-f). Regions 1-4 correspond to the upper left, upper right, lower left and lower right lesions, respectively, in Fig. 2.
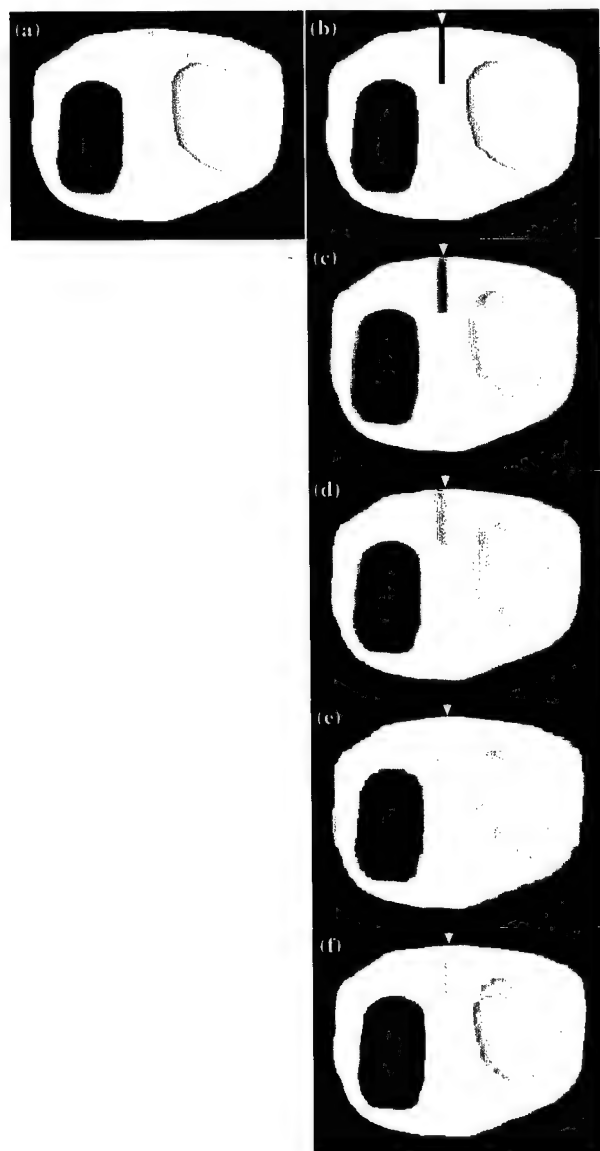
Figure 4: Non-Fourier Encoding Applied to Interventional MRI: (a)-(b) The reference and dynamic images, respectively, reconstructed using 256 phase encodings. The remaining images were reconstructed using 32 dynamic encodings with different encoding techniques: (c) phase, (d) orthogonal wavelet, (e) biorthogonal wavelet and (f) SVD. The phase, wavelet and SVD encoding directions are horizontal. The arrow indicates the center of the needle track. Note the apparent displacement of the needle center in the SVD reconstruction.
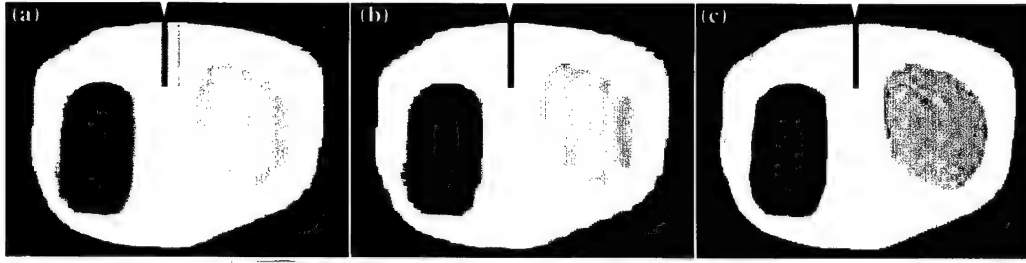
Figure 5: Optimal Non-Fourier Encoding: Dynamic image reconstructed with 32 optimal encodings as derived from the dynamic image itself using (a) orthogonal wavelet, (b) biorthogonal wavelet and (c) SVD. The wavelet and SVD encoding directions are horizontal, and the arrow indicates the center of the needle track. Note the improvement over the images in Figs. 4(d)-(f),respectively, which were reconstructed using the 32 sub-optimal encodings as determined from the reference image in Fig. 4(a).
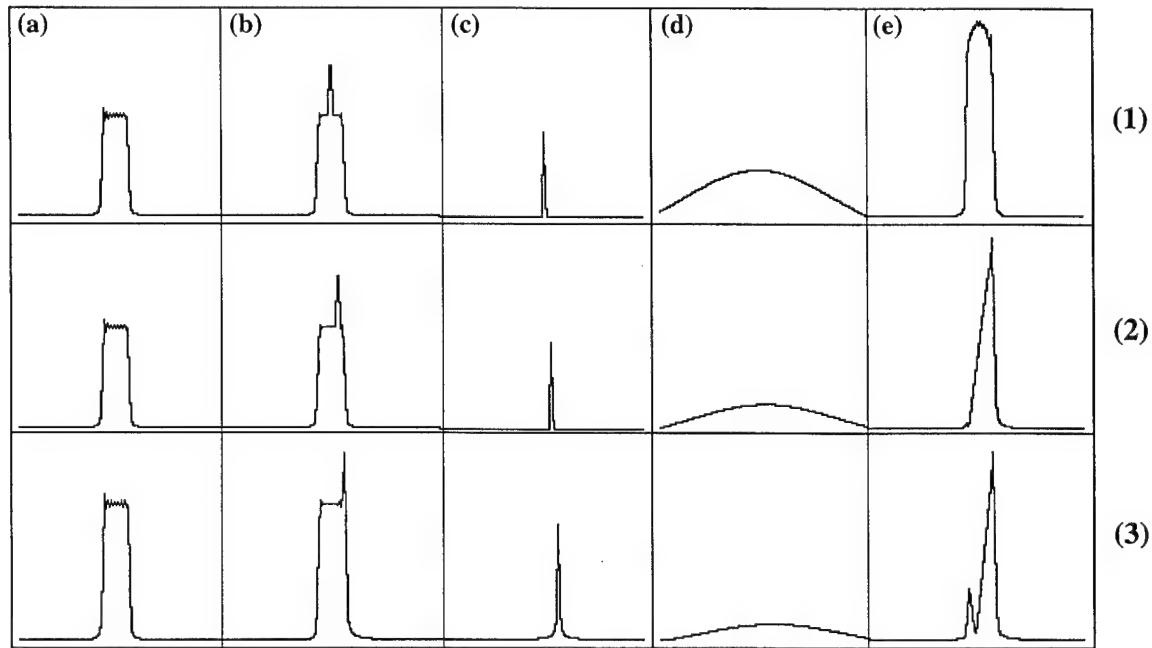
Figure 6: PSF Profiles with Baseline Reference: Rows 1-3 show the PSF results for a delta function change that is centered in the reference boxcar, shifted by one-fourth the width of the reference boxcar from the center, and shifted by just under one-half (0.49) the width of the reference boxcar from the center, respectively. The width of the reference boxcar was 0.03125 (FOV=1), but only the center fourth of the plot is shown for better visualization. (a)-(c) The baseline reference image, the dynamic image, and the point change reconstructed using 512 phase encodings. (d)-(e) The point change reconstructed using Fourier-keyhole (or, equivalently, zero-padded Fourier series) and RIGR with 8 dynamic encodings. Note that (a)-(c) are on a different scale than (d)-(e).
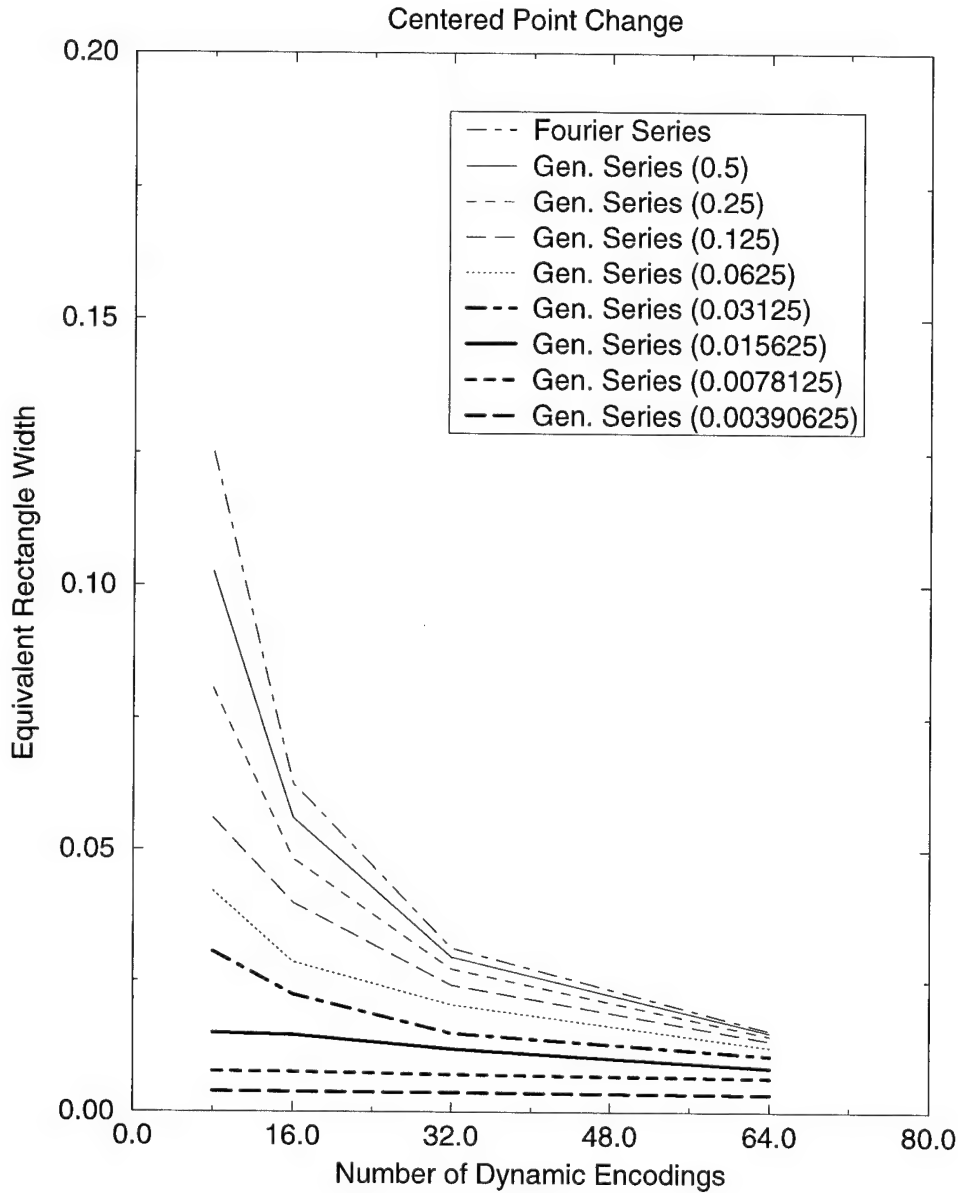
Figure 7: PSF vs Number of Dynamic Encodings: This plot shows the relationship between the width of the PSF and the number of dynamic encodings used for Fourier-keyhole (or, equivalently, the zero-padded Fourier series) and RIGR. In the simulations used to generate this plot, the point change was centered in the reference boxcar. Note the reduced PSF width of RIGR as compared to Fourier-keyhole for all reference boxcar widths and all numbers of dynamic encodings.
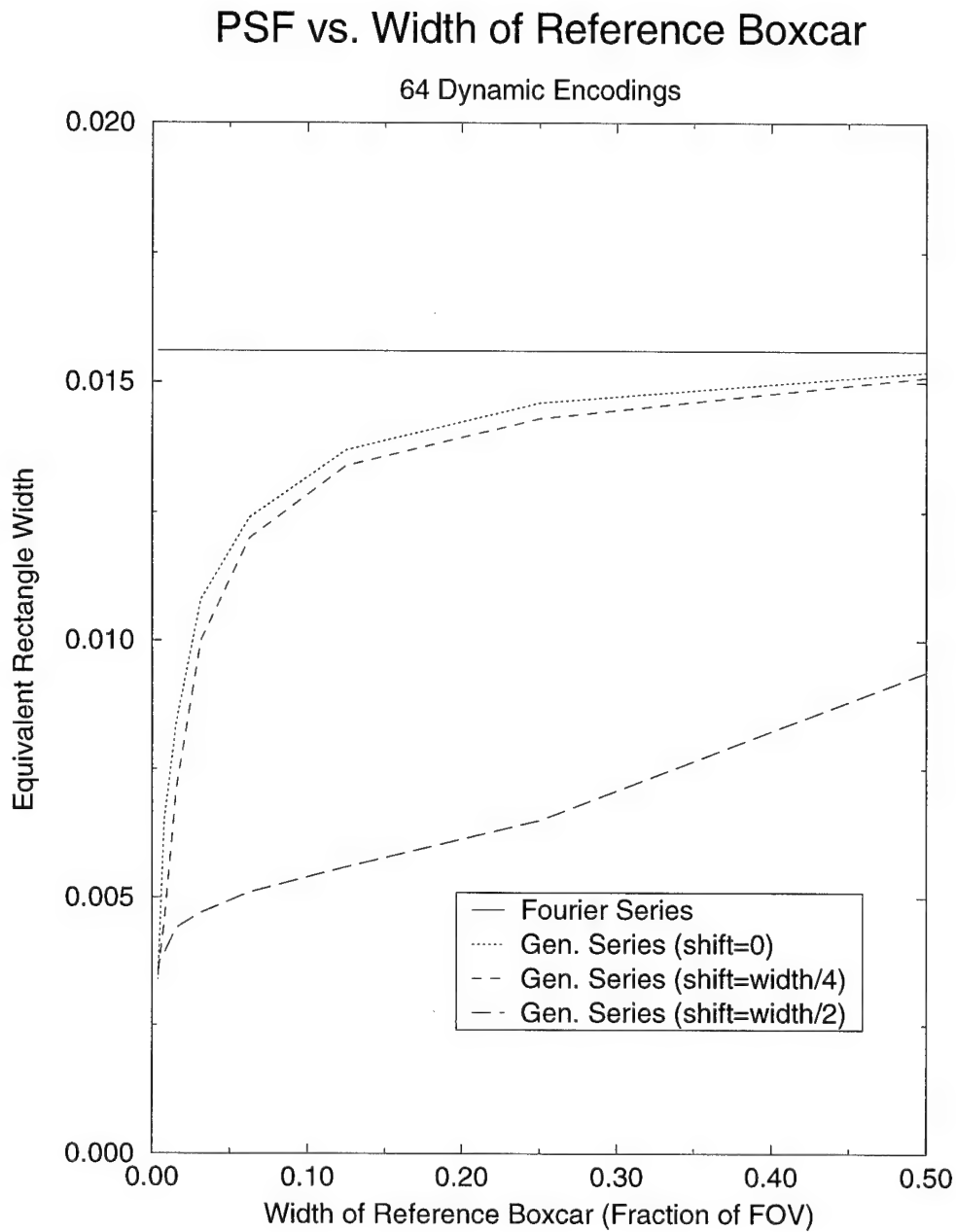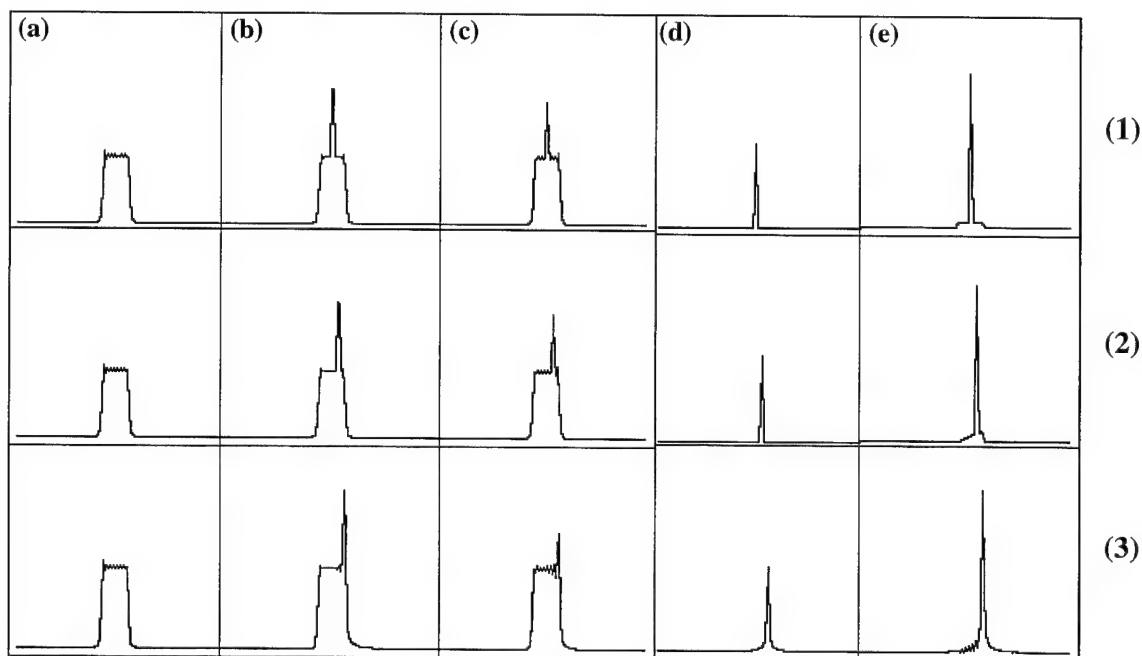
Figure 8: PSF vs Width of Reference Boxcar: This plot shows the relationship between the width of the PSF and the width of the reference boxcar for Fourier-keyhole (or, equivalently, the zero-padded Fourier series) and RIGR for three locations of the point change. The simulations to generate this plot used 64 dynamic encodings.

Figure 9: PSF Profiles with Active Reference: Rows 1-3 show the PSF results for a delta function change that is centered in the reference boxcar, shifted by one-fourth the width of the reference boxcar from the center, and shifted by just under one-half (0.49) the width of the reference boxcar from the center, respectively. The width of the reference boxcar was 0.03125 (FOV=1), but only the center fourth of the plot is shown for better visualization. (a)-(d) The baseline reference image, the active reference image, the dynamic image, and the point change reconstructed using 512 phase encodings. (e) The point change reconstructed using RIGR with the active reference image and 8 dynamic encodings. Note that (a)-(c) are on a different scale than (d)-(e).
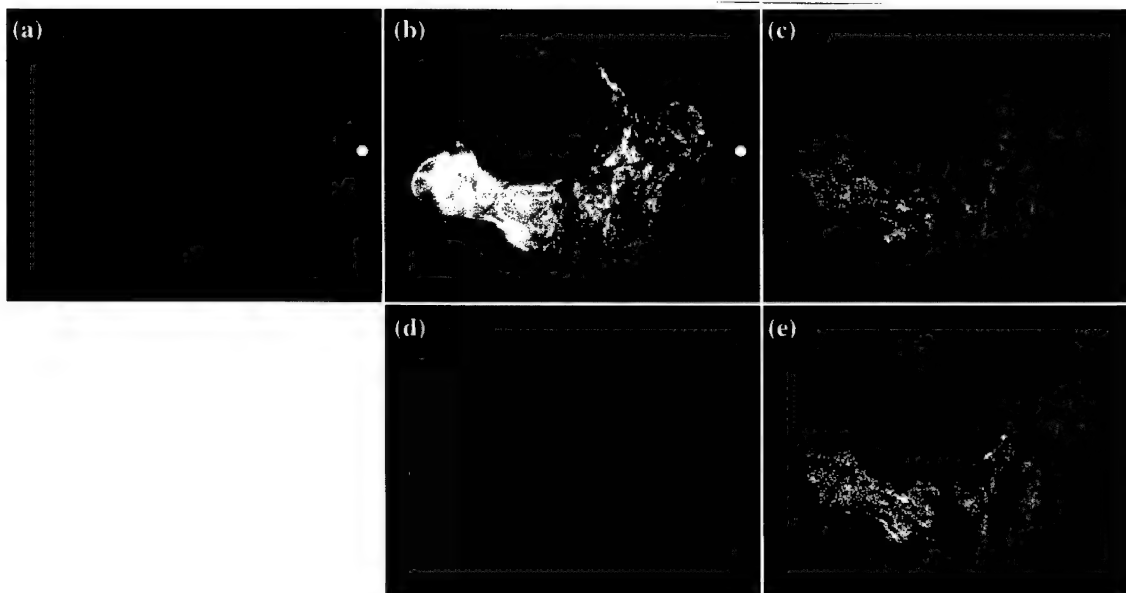
Figure 10: Dynamic Change Images: (a)-(c) The reference and dynamic images and the difference between the two, respectively, reconstructed using 256 phase encodings. (d)-(e) The difference image reconstructed using 32 dynamic encodings with Fourier-keyhole (or, equivalently, zero-padded Fourier series) and RIGR, respectively. Note the improved reconstruction of the dynamic changes with the RIGR method.
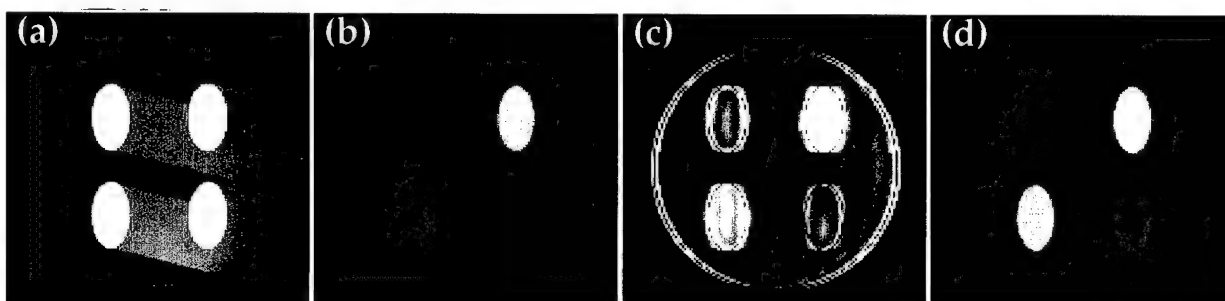

Figure 11: Keyhole Data Inconsistency Artifact: (a)-(b) The reference and dynamic images, respectively, reconstructed using 128 phase encodings. (c)-(d) The dynamic image reconstructed with 16 dynamic encodings using Fourier-keyhole and RIGR, respectively. The phase encoding direction is horizontal. Note the edge artifacts that appear in the Fourier-keyhole image.
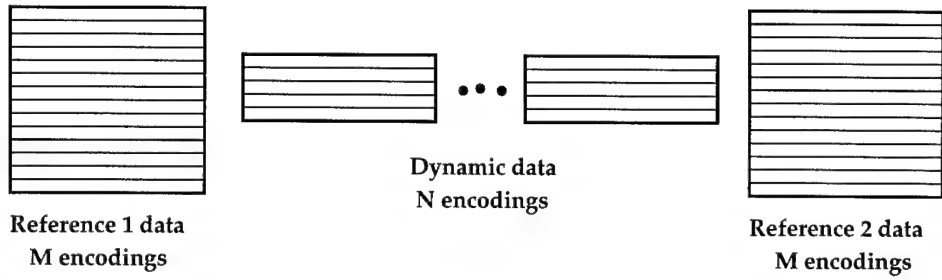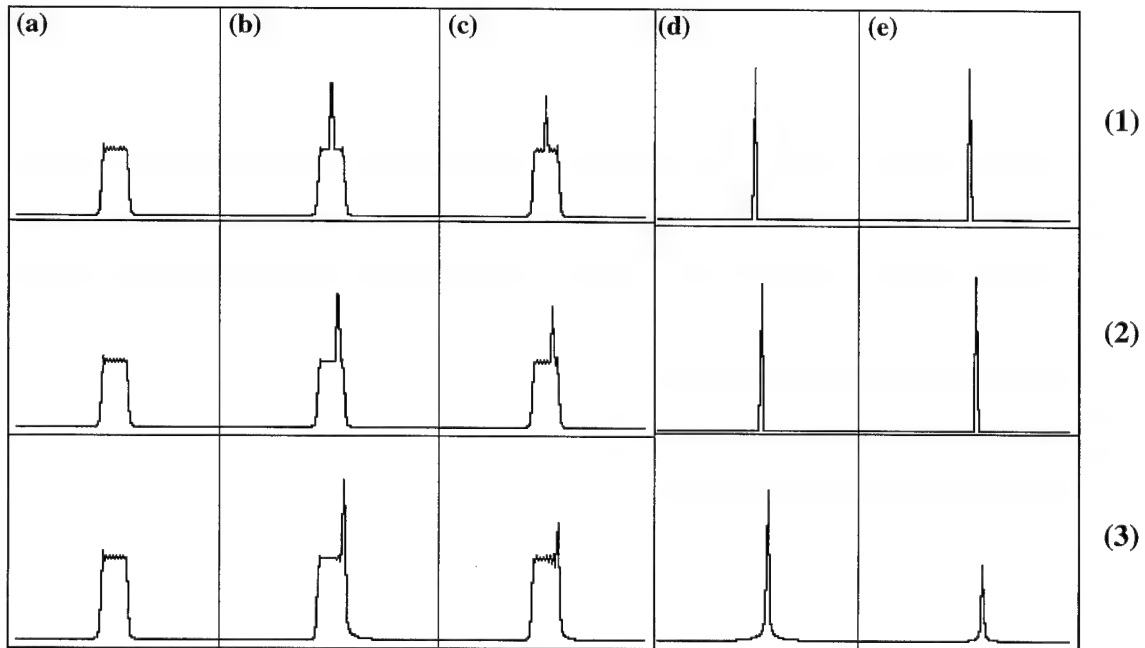
Figure 12: Data Acquisition Strategy for TRIGR

Figure 13: PSF Profiles For TRIGR: Rows 1-3 show the PSF results for a delta function change that is centered in the reference boxcar, shifted by one-fourth the width of the reference boxcar from the center, and shifted by just under one-half (0.49) the width of the reference boxcar from the center, respectively. The width of the reference boxcar was 0.03125 (FOV=1), but only the center fourth of the plot is shown for better visualization. (a)-(d) The baseline reference, active reference, dynamic image, and the point change image, respectively, reconstructed using 512 phase encodings. (e) The point change reconstructed using TRIGR and 8 dynamic encodings. Note that (a)-(c) are on a different scale than (d)-(e).
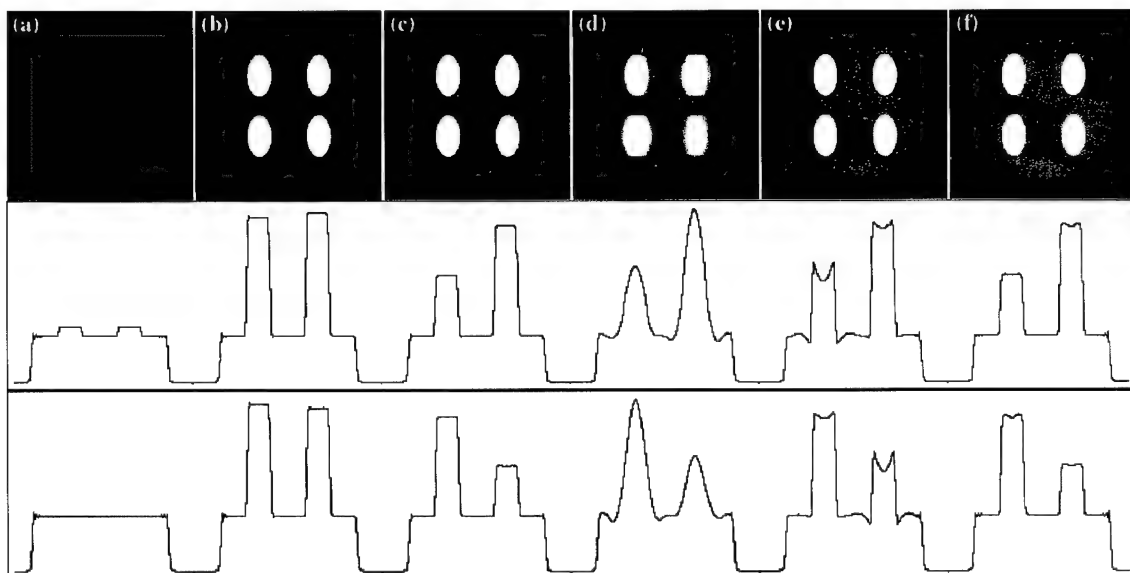
Figure 14: TRIGR with Complete Background Suppression: Images (row 1) and profiles through the upper and lower set of lesions (rows 2-3, respectively). (a)-(c) The baseline reference, active reference and dynamic images, respectively, reconstructed using 128 phase encodings. (d)-(e) The dynamic image reconstructed using 16 dynamic encodings with RIGR using the baseline and active reference images, respectively. (f) The dynamic image reconstructed using 16 dynamic encodings with TRIGR.
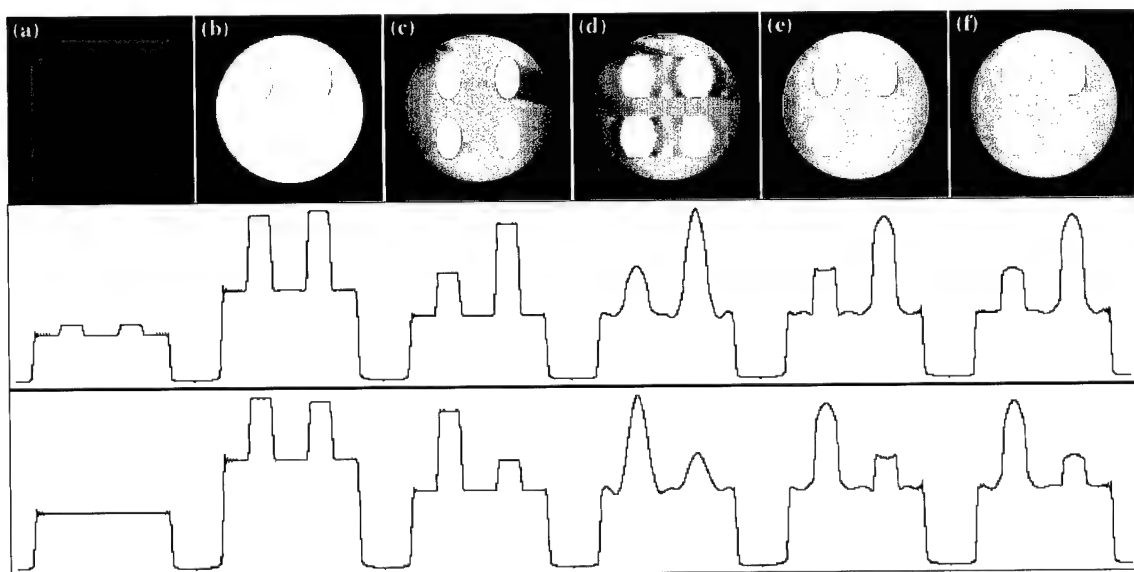

Figure 15: TRIGR with Incomplete Background Suppression: Images (row 1) and profiles through the upper and lower set of lesions (rows 2-3, respectively). (a)-(c) The baseline reference, active reference and dynamic images, respectively, reconstructed using 128 phase encodings. (d)-(e) The dynamic image reconstructed using 16 dynamic encodings with RIGR using the baseline and active reference images, respectively. (f) The dynamic image reconstructed using 16 dynamic encodings with TRIGR.
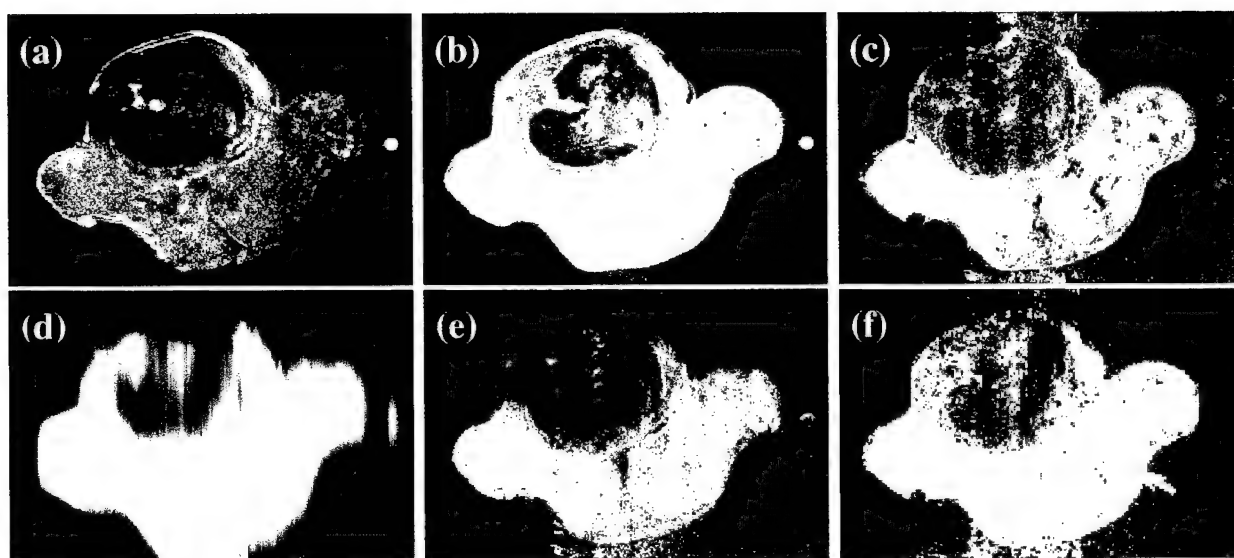
Figure 16: TRIGR Applied to Contrast-Enhanced Dynamic Imaging Experiment on Rat: (a)-(b) The precontrast and postcontrast reference images, respectively, reconstructed using 256 phase encodings. (c) The difference image between the dynamic image (not shown) and the precontrast reference image, reconstructed using 256 phase encodings. (d)-(f) The difference image reconstructed using 8 dynamic encodings with Fourier-keyhole, the original RIGR method and the TRIGR method, respectively. In the TRIGR image, note the improved delineation of the internal details of the tumor, such as those indicated by the arrows.
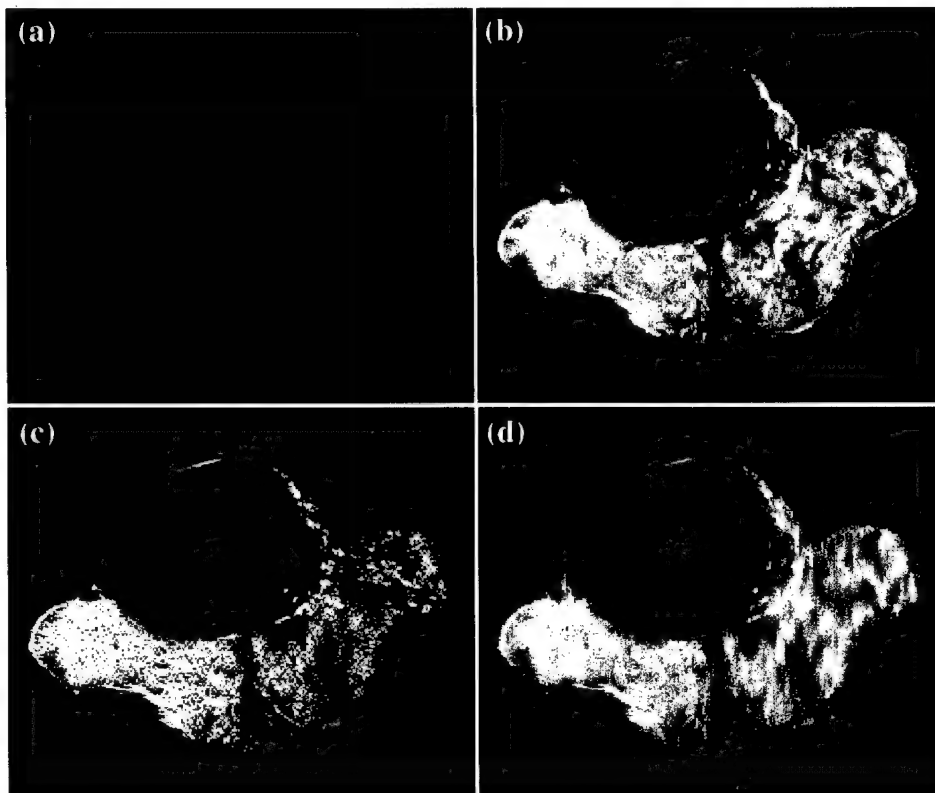
Figure 17: Explicit Edge Information with Precontrast Reference Image: (a)-(b) The original precontrast reference and dynamic images, respectively, reconstructed using 256 phase encodings. (c)-(d) The dynamic image reconstructed using 32 dynamic encodings with the original RIGR method and the RIGR method with explicit edge information, respectively.
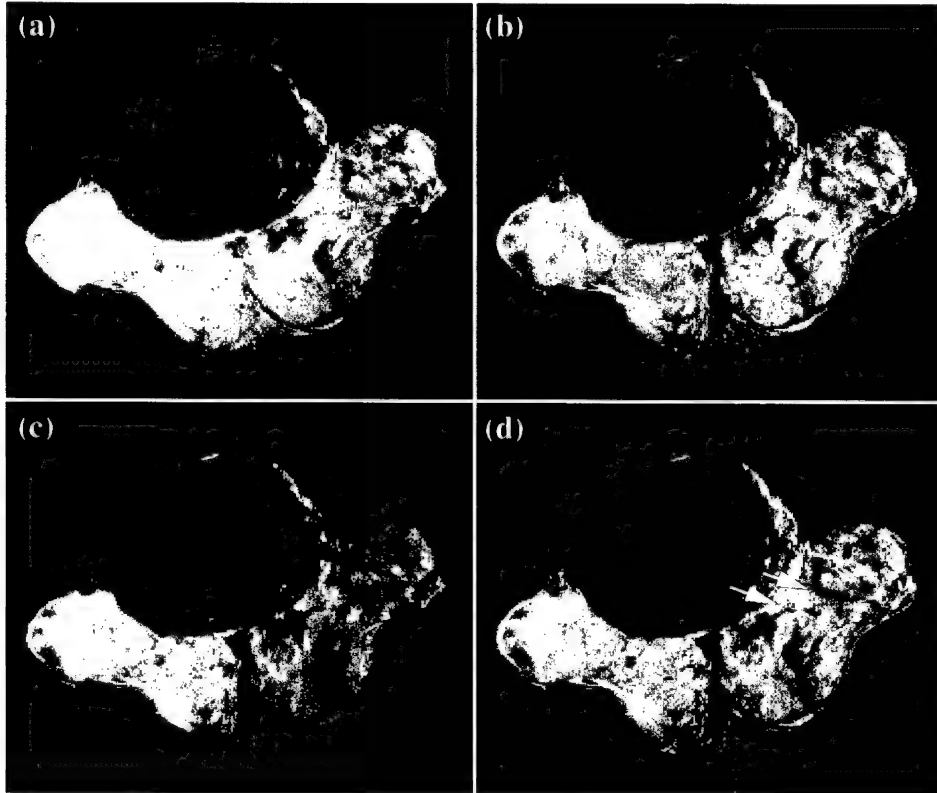
Figure 18: Explicit Edge Information with Postcontrast Reference Image: (a)-(b) The original postcontrast reference and dynamic images, respectively, reconstructed using 256 phase encodings. (c)-(d) The dynamic image reconstructed using 32 dynamic encodings with the original RIGR method and the RIGR method with explicit edge information, respectively.
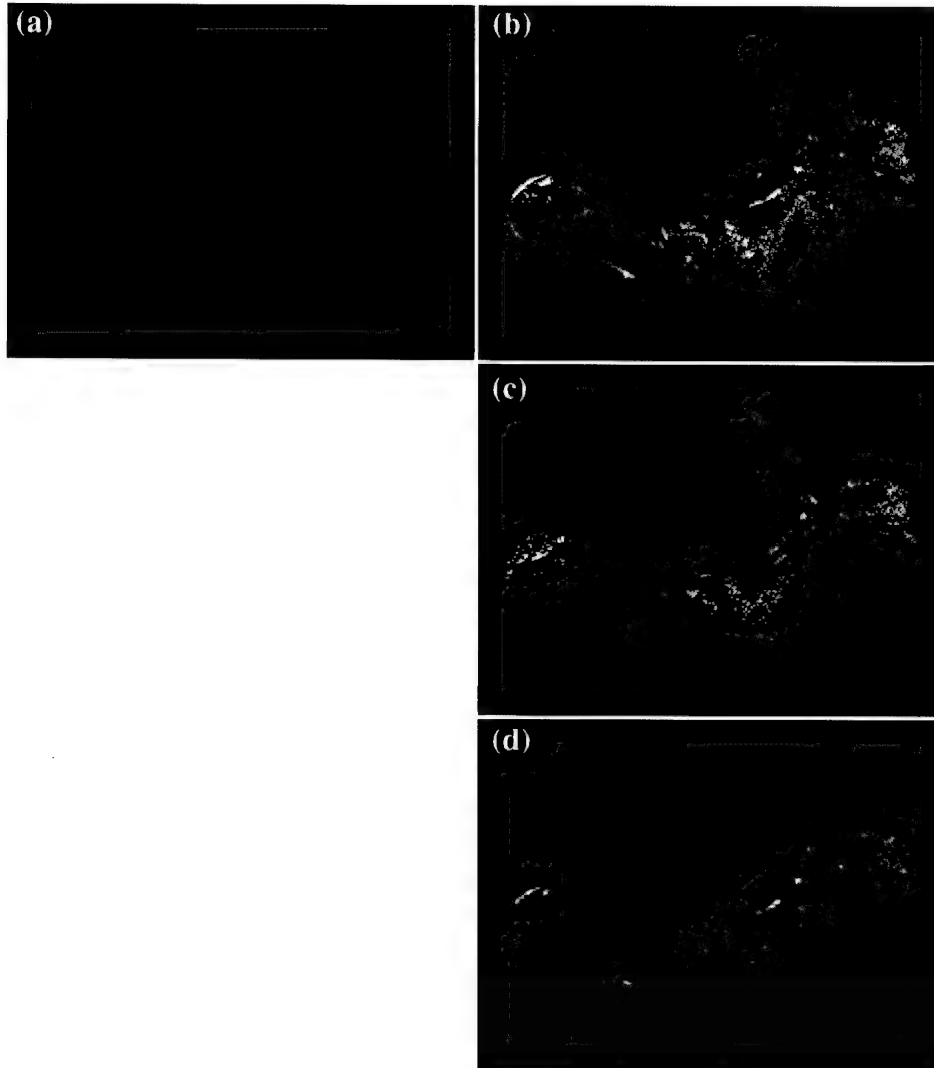
Figure 19: Motion Corrected Dynamic Images: (b)-(d) were reconstructed using the GS model with (a) as the reference image and 32 dynamic encodings. (b) The dynamic image that results with no motion between the reference and dynamic data sets. The remaining images show the dynamic image reconstructed with a 5 pixel shift in the phase-encoding direction (vertical), a -3 pixel shift in the frequency-encoding direction (horizontal) and a 3 degree clockwise rotation between the reference and dynamic data sets. (c)-(d) The dynamic images that result with no motion correction and with the proposed method, respectively. Note the reduced motion artifacts in (d) as compared to (c).

References

[1] S. H. Heywang, A. Wolf, E. Pruss, T. Hilbertz, W. Eiermann, and W. Permanet-ter, "MR imaging of the breast with Gd-DTPA: Use and limitations," *Radiology*, vol. 171, pp. 95–103, 1989.

[2] W. A. Kaiser, "MR imaging examination of both breasts within 6 minutes: Technique and first results," in *Proc. RSNA 75th Ann. Meeting*, (Chicago, IL), p. 164, November/December 1989.

[3] W. A. Kaiser, "MR imaging of the breast: Optimal imaging technique, results, limitations and histopathologic correlation," in *Proc. RSNA 75th Ann. Meeting*, (Chicago, IL), p. 230, November/December 1989.

[4] W. A. Kaiser and O. Mittelmeier, "Breast-tissue differentiation by MRI: Results of 361 examinations in 5 years," in *Tissue Characterization in MR Imaging* (H. P. Higer and G. Bielke, eds.), pp. 254–257, Springer-Verlag, 1990.

[5] W. A. Kaiser, "MRM promises earlier breast cancer diagnosis," *Diagnostic Imaging*, pp. 88–93, Sept. 1992.

[6] S. E. Harms, D. P. Flamig, K. L. Hesley, and W. P. Evans, "Magnetic resonance imaging of the breast," *Magn. Reson. Q.*, vol. 8, no. 3, pp. 139–155, 1992.

[7] S. E. Harms and D. P. Flamig, "Breast: Visualizing Ca not seen by radiography," *Body MRI*, pp. 20–24, June 1993.

[8] S. E. Harms and D. P. Flamig, "MR imaging of the breast," *J. Magn. Reson. Imag.*, vol. 3, pp. 277–283, January/February 1993.

[9] J. P. Stack, O. M. Redmond, M. B. Codd, P. A. Dervan, and J. T. Ennis, "Breast disease: Tissue characterization with Gd-DTPA enhancement profiles," *Radiology*, vol. 174, pp. 491–494, 1990.

[10] W. A. Kaiser and E. Zeitler, "MR imaging of the breast: Fast imaging sequences with and without Gd-DTPA, preliminary observations," *Radiology*, vol. 170, pp. 681–686, 1989.

[11] B. A. Porter and J. P. Smith, "MRI enhances breast cancer detection and staging," *MR*, pp. 18–26,35, September/October 1993.

[12] E. Furman-Haran, R. Margalit, A. F. Maretzek, and H. Degani, "Angiogenic response of MCF7 human breast cancer to hormonal treatment: Assessment by dynamic GdDTPA-enhanced MRI at high spatial resolution," *J. Magn. Reson. Imag.*, vol. 6, pp. 195–202, January/February 1996.

[13] Y. Yamashita, M. Harada, M. Torashima, M. Takahashi, K. Miyazaki, N. Tanaka, and H. Okamura, "Dynamic MR imaging of recurrent postoperative cervical cancer," *J. Magn. Reson. Imag.*, vol. 6, pp. 167–171, January/February 1996.

[14] D. B. Twieg, "The k-trajectory formulation of the NMR imaging process with applications in analysis and synthesis of imaging methods," *Med. Phys.*, vol. 10, pp. 610–621, 1983.

[15] Z.-P. Liang and P. C. Lauterbur, "Improved temporal/spatial resolution in functional imaging through generalized series reconstruction," in *Works-in-Progress Proc. Soc. Magn. Reson. Imag. 10th Ann. Meeting*, (New York, NY), p. S15, Aug. 1992.

[16] Z.-P. Liang and P. C. Lauterbur, "An efficient method for dynamic magnetic resonance imaging," *IEEE Trans. Med. Imaging*, vol. 13, pp. 677–686, Dec. 1994.

[17] J. B. Weaver and D. M. Healy, Jr., "New MRI acquisition techniques using the window Fourier transforms and the wavelet transforms," in *Proc. Soc. Magn. Reson. Med. 9th Ann. Meeting*, (New York, NY), p. 414, Aug. 1990.

[18] J. B. Weaver, Y. Xu, D. Crean, and D. M. Healy, "Wavelet encoding in MR imaging," in *Proc. Soc. Magn. Reson. Med. 10th Ann. Meeting*, (San Francisco, CA), p. 182, Aug. 1991.

[19] J. B. Weaver, Y. Xu, D. Crean, and D. M. Healy, "Imaging times in window Fourier transform imaging," in *Proc. Soc. Magn. Reson. Med. 10th Ann. Meeting*, (San Francisco, CA), p. 857, Aug. 1991.

[20] D. M. Healy and J. B. Weaver, "Two applications of wavelet transforms in magnetic resonance imaging," *IEEE Trans. Inf. Theory*, vol. 38, pp. 840–860, 1992.

[21] X. Hu, A. H. Tewfik, and H. Garnaoui, "A new wavelet based MR imaging technique," in *Proc. Soc. Magn. Reson. Med. 11th Ann. Meeting*, (Berlin, Germany), p. 432, Aug. 1992.

[22] L. P. Panych, P. D. Jakab, and F. A. Jolesz, "Progress towards real-time adaptive imaging using wavelet transform encoding," in *Proc. Soc. Magn. Reson. Med. 11th Ann. Meeting*, (Berlin, Germany), p. 4513, Aug. 1992.

[23] L. P. Panych and P. D. Jakab, "Wavelet encoding in the section-select dimension," in *Proc. Soc. Magn. Reson. Imag. 10th Ann. Meeting*, (New York, NY), p. 90, Apr. 1992.

[24] J. B. Weaver, Y. Xu, D. M. Healy, and J. R. Driscoll, "Wavelet-encoded MR imaging," *Magn. Reson. Med.*, vol. 24, pp. 275–287, 1992.

[25] J. B. Weaver, D. M. Healy, Jr., D. Crean, and Y. Xu, "Wavelet encoding with smooth wavelets: Short RF pulses," in *Proc. Soc. Magn. Reson. Med. 11th Ann. Meeting*, (Berlin, Germany), p. 4264, Aug. 1992.

[26] J. B. Weaver, D. M. Healy, Jr., and Y. Xu, "SNR for wavelet encoded MR," in *Proc. Soc. Magn. Reson. Med. 11th Ann. Meeting*, (Berlin, Germany), p. 3822, Aug. 1992.

[27] J. B. Weaver and D. M. Healy, Jr., "Adaptive wavelet encoding in cardiac imaging," in *Proc. Soc. Magn. Reson. Med. 11th Ann. Meeting*, (Berlin, Germany), p. 3906, Aug. 1992.

[28] J. M. Hanson, Z.-P. Liang, and P. C. Lauterbur, "A new method for fast dynamic imaging using wavelet transforms," in *Proc. Soc. Magn. Reson. Med. 12th Ann. Meeting*, (New York, NY), p. 712, Aug. 1993.

[29] K. Oshio, L. P. Panych, and F. A. Jolesz, "Wavelet encoded MR imaging (implementation)," in *Proc. Soc. Magn. Reson. Med. 12th Ann. Meeting*, (New York, NY), p. 1213, Aug. 1993.

[30] L. P. Panych, P. D. Jakab, and F. A. Jolesz, "An implementation of wavelet-encoded MR imaging," in *Proc. Soc. Magn. Reson. Imag. 10th Ann. Meeting*, (New York, NY), p. 26, Apr. 1993.

[31] L. P. Panych, P. D. Jakab, and F. A. Jolesz, "Implementation of wavelet-encoded MR imaging," *J. Magn. Reson. Imag.*, vol. 3, pp. 649–655, 1993.

[32] R. D. Peters and M. L. Wood, "Practical considerations for the implementation of wavelet encoding in MRI," in *Proc. Soc. Magn. Reson. Med. 12th Ann. Meeting*, (New York, NY), p. 1212, Aug. 1993.

[33] L. P. Panych and F. A. Jolesz, "A dynamically adaptive imaging algorithm for wavelet-encoded MRI," *Magn. Reson. Med.*, vol. 32, pp. 738–748, 1994.

[34] L. P. Panych and F. A. Jolesz, "Theoretical comparison of resolution in wavelet and Fourier encoded MR images," in *Proc. Soc. Magn. Reson. 2nd Ann. Meeting*, (San Francisco, CA), p. 776, Aug. 1994.

[35] L. P. Panych and F. A. Jolesz, "Design of optimal wavelet bases for wavelet encoded MRI," in *Proc. Soc. Magn. Reson. 2nd Ann. Meeting*, (San Francisco, CA), p. 777, Aug. 1994.

[36] N. Gelman, M. L. Wood, and R. D. Peters, "Three dimensional gradient echo imaging using wavelet encoding," in *Proc. Soc. Magn. Reson. 3rd Ann. Meeting*, (Nice, France), p. 662, Aug. 1995.

[37] R. D. Peters and M. L. Wood, "Multilevel wavelet-encoded MR imaging," in *Proc. Soc. Magn. Reson. 3rd Ann. Meeting*, (Nice, France), p. 194, Aug. 1995.

[38] N. Gelman and M. L. Wood, "Wavelet encoding for improved SNR and retrospective slice thickness adjustment," in *Proc. Int. Soc. Magn. Reson. Med. 4th Ann. Meeting*, (New York, NY), p. 1535, April/May 1996.

[39] W.-L. Hwang, N.-K. Chen, C. Chen, and H. N. Yeung, "Application of wavelet decomposition in dynamic MRI," in *Proc. Int. Soc. Magn. Reson. Med. 4th Ann. Meeting*, (New York, NY), p. 1650, April/May 1996.

[40] L. P. Panych, "Theoretical comparison of Fourier and wavelet encoding in magnetic resonance imaging," *IEEE Trans. Med. Imaging*, vol. 15, pp. 141–153, Apr. 1996.

[41] R. D. Peters and M. L. Wood, "Multilevel wavelet-transform encoding in MRI," *J. Magn. Reson. Imag.*, vol. 6, pp. 529–540, 1996.

[42] Y. Cao and D. N. Levin, "On the relationship between feature-recognizing MRI and MRI encoded by singular value decomposition," *Magn. Reson. Med.*, vol. 33, pp. 140–142, Jan. 1995.

[43] Y. Cao, D. N. Levin, and L. Yao, "Locally focused MRI," *Magn. Reson. Med.*, vol. 34, pp. 858–867, Dec. 1995.

[44] L. P. Panych, C. Oesterle, G. P. Zientara, and J. Hennig, "Implementation of a fast gradient-echo SVD encoding technique for dynamic imaging," in *Proc. Soc. Magn. Reson. 3rd Ann. Meeting*, (Nice, France), p. 663, Aug. 1995.

[45] L. P. Panych, C. Oesterle, G. P. Zientara, and J. Hennig, "Implementation of a fast gradient-echo SVD encoding technique for dynamic imaging," *Magn. Reson. Med.*, vol. 35, pp. 554–562, 1995.

[46] L. P. Panych, W. E. Kyriakos, G. P. Zientara, and F. A. Jolesz, "Dynamically adaptive MRI methods for following change occuring within a reduced field-of-view," in *Proc. Soc. Magn. Reson. 3rd Ann. Meeting*, (Nice, France), p. 193, Aug. 1995.

[47] L. P. Panych, P. Saiviroonporn, R. V. Mulkern, G. P. Zientara, and F. A. Jolesz, "Non-Fourier encoding with multiple spin echoes," in *Proc. Int. Soc. Magn. Reson. Med. 4th Ann. Meeting*, (New York, NY), p. 115, April/May 1996.

[48] L. P. Panych, P. Saiviroonporn, G. P. Zientara, and F. A. Jolesz, "Implementation of a 3D interleaved echo-planar method for SVD encoded MRI," in *Proc. Int. Soc. Magn. Reson. Med. 4th Ann. Meeting*, (New York, NY), p. 387, April/May 1996.

[49] P. Saiviroonporn, G. P. Zientara, L. P. Panych, and F. A. Jolesz, "Real-time computations for dynamically adaptive SVD encoded MRI," in *Proc. Soc. Magn. Reson. 3rd Ann. Meeting*, (Nice, France), p. 665, Aug. 1995.

[50] G. P. Zientara, L. P. Panych, and F. A. Jolesz, "Dynamically adaptive MRI with encoding by singular value decomposition," *Magn. Reson. Med.*, vol. 32, pp. 268–274, 1994.

[51] G. P. Zientara, L. P. Panych, and F. A. Jolesz, "Keyhole SVD encoded MRI," in *Proc. Soc. Magn. Reson. 2nd Ann. Meeting*, (San Francisco, CA), p. 778, Aug. 1994.

[52] G. P. Zientara, L. P. Panych, and F. A. Jolesz, "Multi-resolution SVD encoding for dynamically adaptive MRI," in *Proc. Soc. Magn. Reson. 2nd Ann. Meeting,* (San Francisco, CA), p. 800, Aug. 1994.

[53] G. P. Zientara, L. P. Panych, and F. A. Jolesz, "Lanczos spatial encodings for dynamically adaptive MRI," in *Proc. Soc. Magn. Reson. 3rd Ann. Meeting,* (Nice, France), p. 664, Aug. 1995.

[54] G. P. Zientara, L. P. Panych, P. Saiviroonporn, and F. A. Jolesz, "MR fluoroscopy using near-optimal adaptive spatial encoding," in *Proc. Int. Soc. Magn. Reson. Med. 4th Ann. Meeting,* (New York, NY), p. 1495, April/May 1996.

[55] K. S. Arun, "Fundamentals of digital signal and spectral analysis." ECE 413 Class Book, Dept. of Electrical and Computer Engineering, Univ. of Illinois at Urbana-Champaign, Urbana, IL, Spring 1992.

[56] I. Daubechies, "Orthonormal bases of compactly supported wavelets," *Comm. Pure Appl. Math.,* vol. XLI, pp. 909–996, 1988.

[57] M. Antonini, M. Barlaud, P. Mathieu, and I. Daubechies, "Image coding using wavelet transform," *IEEE Trans. Image Proc.,* vol. 1, pp. 205–220, Apr. 1992.

[58] J. D. Villasenor, B. Belzer, and J. Liao, "Wavelet filter evaluation for image compression," *IEEE Trans. Image Proc.,* vol. 2, pp. 1053–1060, Aug. 1995.

[59] J. J. van Vaals, H. H. Tuithof, and W. T. Dixon, "Increased time resolution in dynamic imaging," in *Proc. Soc. Magn. Reson. Imag. 10th Ann. Meeting,* (New York, NY), p. 44, Aug. 1992.

[60] J. E. Bishop, I. Soutar, W. Kucharczyk, and D. B. Plewes, "Rapid sequential imaging with shared-echo fast spin-echo MR imaging," in *Works-in-Progress Proc. Soc. Magn. Reson. Imag. 10th Ann. Meeting,* (New York, NY), p. S22, Aug. 1992.

[61] S. Mallat and S. Zhong, "Compact image coding from edges with wavelets," in *Proc.,* Int. Conf. Acoust. Speech Sig. Proc., (Toronto), pp. 2745–2748, 1991.

[62] S. Mallat and S. Zhong, "Characterization of signals from multiscale edges," *IEEE Trans. Patt. Anal. Mach. Intell.,* vol. 14, pp. 710–732, July 1992.

[63] L. Du, J. Lee, K. Hoppel, and S. A. Mango, "Segmentation of SAR images using the wavelet transform," *Int. J. Imag. Sys. and Tech.*, vol. 4, pp. 319–326, 1992.

[64] N. Ahuja, "A transform for detection of multiscale image structure," in *Proc. DARPA Image Understanding Workshop*, (Washington, DC), pp. 893–902, Apr. 1993.

[65] N. Ahuja, "A transform for detection of multiscale image structure," in *Proc. Comp. Vision Patt. Recog.*, (New York, NY), pp. 780–781, June 1993.

[66] Z.-P. Liang, *Constrained Reconstruction from Incomplete and Noisy Data: A New Parametric Approach.* PhD thesis, Case Western Reserve University, Cleveland, May 1989. Department of Biomedical Engineering.

[67] R. L. Ehman and J. P. Felmlee, "Adaptive technique for high-definition MR imaging of moving structures," *Radiology*, vol. 173, no. 1, pp. 258–263, 1989.

[68] Y. Wang, R. C. Grimm, S. J. Riederer, and R. L. Ehman, "Algorithms to extract motion information from navigator echoes," in *Proc. Soc. Magn. Reson. 3rd Ann. Meeting*, (Nice, France), p. 751, Aug. 1995.

[69] Z. W. Fu, Y. Wang, R. C. Grimm, P. J. Rossman, J. P. Felmlee, S. J. Riederer, and R. L. Ehman, "Orbital navigator echoes for motion measurements in magnetic resonance imaging," *Magn. Reson. Med.*, vol. 34, pp. 746–753, 1995.

[70] Y. Wang, R. C. Grimm, J. P. Felmlee, S. J. Riederer, and R. L. Ehman, "Algorithms for extracting motion information from navigator echoes," *Magn. Reson. Med.*, vol. 36, pp. 117–123, 1996.

[71] C. C. Lee, C. R. Jack, Jr., R. C. Grimm, P. J. Rossman, J. P. Felmlee, R. L. Ehman, and S. J. Riederer, "Real-time adaptive motion correction in functional MRI," *Magn. Reson. Med.*, vol. 36, pp. 436–444, 1996.

7 Appendix A - Acronyms

BMRL - Biomedical Magnetic Resonance Laboratory

FOV - Field of View

ISMRM - International Society for Magnetic Resonance in Medicine

LPA - Localized Polynomial Approximation

MR - Magnetic Resonance

MRI - Magnetic Resonance Imaging

PSF - Point Spread Function

RIGR - Reduced-encoding Imaging by Generalized-series Reconstruction

RSNA - Radiological Society of North America

SMR - Society of Magnetic Resonance

SMRI - Society of Magnetic Resonance Imaging

SMRM - Society of Magnetic Resonance in Medicine

SNR - Signal to Noise Ratio

SVD - Singular Value Decomposition

TRIGR - Two reference Reduced-encoding Imaging by Generalized-series Reconstruction

8 Appendix B - List of Personnel

1. Jill Marie Hanson

9   Appendix C - Bibliography of Publications

[1] J. M. Hanson, Z.-P. Liang, and P. C. Lauterbur, "Improved RIGR dynamic imaging using explicit boundary constraints with application to breast imaging," in *Proc. Soc. Magn. Reson. 3rd Ann. Meeting*, (Nice, France), p. 1596, Aug. 1995.

[2] J. M. Hanson, Z.-P. Liang, E. Wiener, and P. C. Lauterbur, "Fast dynamic imaging using two reference images," in *Proc. Soc. Magn. Reson. 3rd Ann. Meeting*, (Nice, France), p. 97, Aug. 1995.

[3] J. M. Hanson, Z.-P. Liang, R. L. Magin, J. L. Duerk, and P. C. Lauterbur, "A comparison of RIGR and SVD dynamic MRI methods," in *Proc. Int. Soc. Magn. Reson. Med. 4th Ann. Meeting*, (New York, NY), p. 118, April/May 1996.

[4] J. M. Hanson, Z.-P. Liang, E. Wiener, and P. C. Lauterbur, "Fast dynamic imaging using two reference images," *Magn. Reson. Med.*, vol. 36, pp. 172–175, July 1996.

[5] J. M. Hanson, Z.-P. Liang, R. L. Magin, J. L. Duerk, and P. C. Lauterbur, "A comparison of RIGR and SVD dynamic MRI methods," *Magn. Reson. Med.*, vol. 38, pp. 161–167, 1997.

[6] J. M. Hanson, *Reduced-encoding dynamic imaging*. PhD thesis, University of Illinois at Urbana-Champaign, Urbana-Champaign, Illinois, 1997. Department of Electrical and Computer Engineering.